DISSERTATION

RADIO FREQUENCY DRIVEN DIRECT CURRENT ELECTRON BEAM SOURCE

Submitted by

Denis M. Shaw

Department of Electrical and Computer Engineering

In partial fulfillment of the requirements

for the Degree of Doctor of Philosophy

Colorado State University

Fort Collins, Colorado

Summer 2007

COLORADO STATE UNIVERSITY

July 9, 2007

WE HEREBY RECOMMEND THAT THE DISSERTATION PREPARED UNDER OUR SUPERVISION BY DENIS M. SHAW ENTITLED RADIO FREQUENCY DIRECT CURRENT ELECTRON BEAM SOURCE BE ACCEPTED AS FULFILLING IN PART THE REQUIREMENTS FOR THE DEGREE OF DOCTOR OF PHILOSOPHY.

Committee on Graduate Work

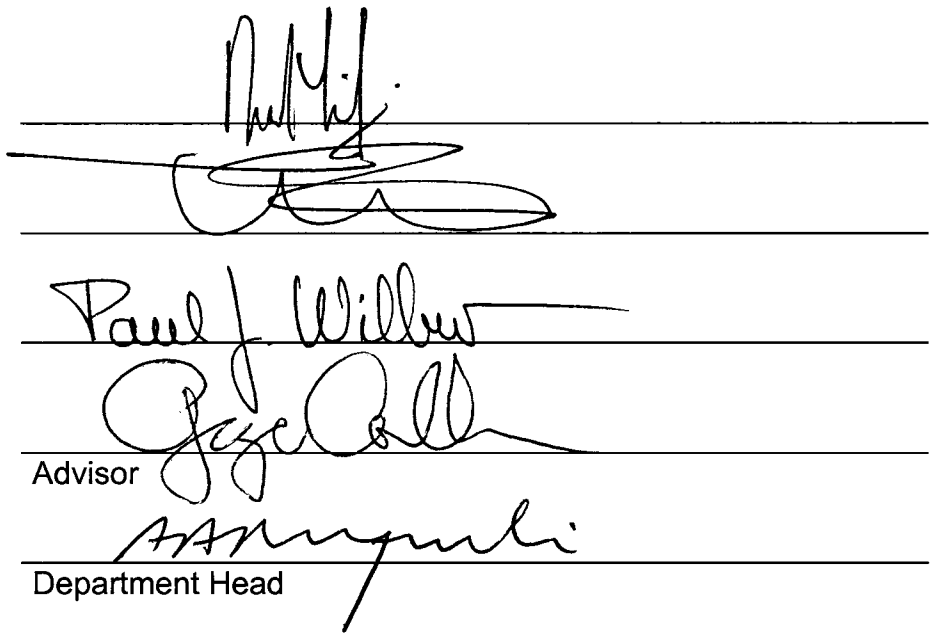

Advisor

Department Head

ABSTRACT OF DISSERTATION

A RADIO FREQUENCY DRIVEN DIRECT CURRENT ELECTRON BEAM SOURCE

A new type of electron beam source employing ion-induced secondary electron emission from cold cathodes is developed for feature charge neutralization during plasma etching. A low pressure (approximately 2 – 20 mTorr) inductively coupled plasma provides ions which impinge on a high secondary electron emission coefficient anodized aluminum (Al_2O_3) cathode surface. A separate 13.56 MHz radio frequency bias voltage is applied to the cathode, which through the rectifying behavior of the plasma sheath provides the effective DC field for both ion impingement and electron beam acceleration. The electron beam energy spectra are measured at a location 14 cm from the cold cathode using a differentially pumped retarding potential analyzer. The measured electron beam energy spectra is related to the time varying cathode sheath potential provided by the rf bias using collisionless Child-Langmuir rf sheath model with good agreement.

The electron beam source is installed on an inductively coupled plasma etcher in an attempt to increase etch pattern transfer fidelity in silicon oxide feature etching. When used during CF_4 plasma etching of 0.45 μm diameter via holes, the electron beam is shown to reduce microtrenching as compared to standard ion-assisted etching, as verified with scanning electron microscopic

photos. A simple electrostatic model is used to explain the etch profile improvement.

Denis M. Shaw
Department of Electrical and Computer Engineering
Colorado State University
Fort Collins, CO 80523
Summer 2007

Table of Contents

List of Figures

Chapter 4

CHAPTER 1

INTRODUCTION

1.1 Project description

Previously, soft vacuum direct current (DC) secondary electron beams were created using abnormal glow DC excitation.[1,2] The prior electron beams had useful but limited application in materials processing, such as polycrystalline film recrystallization, thin film deposition, and photoresist hardening. Major limitations of the prior DC electron beam sources are that conducting electrodes must be used, and the electron beam energy is typically higher than 1 keV and generally not independent of electron current in the DC abnormal glow regime.[3] In order to have efficient electron beam generation, conducting ceramic-metal (cermet) cathodes were generally used, since compared to metal cathodes, the metal oxide ceramic content of cermet cathodes allows much higher secondary electron emission than pure metal.[4] The secondary electron emission coefficient γ is the ratio of emitted secondary electrons to incident ions impinging on a surface, and $\gamma(\text{metal}) \sim 10^{-1}$, whereas $\gamma(\text{metal oxide}) \sim 1$. Both metal and cermet cathodes sputter easily when subjected to ion bombardment, resulting in short cathode lifetimes. Contamination of the plasma by sputtered species from the metal and cermet cathodes is also of concern in many applications.

Secondary electron emission from the cold electrode of capacitively coupled rf plasmas is generally ignored since most of the electron current required to sustain the discharge is thought to be provided by the displacement current through the capacitive sheath.[5] Traditional capacitively coupled plasmas are often termed to operate in the α-mode, where ionization in the bulk discharge occurs by the capacitive rf electron current flowing through the sheath which sustains the discharge. It is known that under proper plasma and electrode conditions, secondary electron emission from the electrodes can play a stronger role in sustaining rf capacitive discharges. This is sometimes referred to as the γ-mode rf discharge.[6] In the γ-mode, secondary electrons emitted from the cathode surface following ion bombardment are accelerated by the sheath electric field toward the bulk plasma. Under conditions where the mean free path for ionization is much smaller than the sheath size, the accelerated secondary electrons undergo many ionizing collisions in the sheath rather than in the bulk plasma. A distinct change in the electrode rf I-V characteristics from the α-mode to the γ-mode rf discharge is generally seen.[7]

Herein, recent experimental observations of the rf γ-mode[8] have led to the development of a new electron beam source which uses a robust, high secondary electron emission coefficient ceramic (Al_2O_3) cathode material. This is the same material that is employed to coat the entire inside surface of plasma etch chambers, and thus is compatible with integrated circuit (IC) plasma etch and other critical plasma processes. The cathode is independently biased using radio frequency (rf) voltage, typically at 13.56 MHz. The bulk plasma in

the new electron beam source is maintained independently of beam formation by a separate inductively coupled plasma (ICP) source, also excited with 13.56 MHz rf voltage. The ICP source coils lie on an open-ended cylinder, providing an open path for electrons accelerated from the disc-shaped cathode located on the top of the cylinder to enter the plasma as shown in Figure 1. By employing the separate ICP apparatus to sustain the bulk plasma, we may operate the rf bias on the cold disc cathode independently from plasma formation and in a lower pressure region ($2 < p < 20$ mTorr) which is typically impossible for efficient capacitive plasma excitation alone.

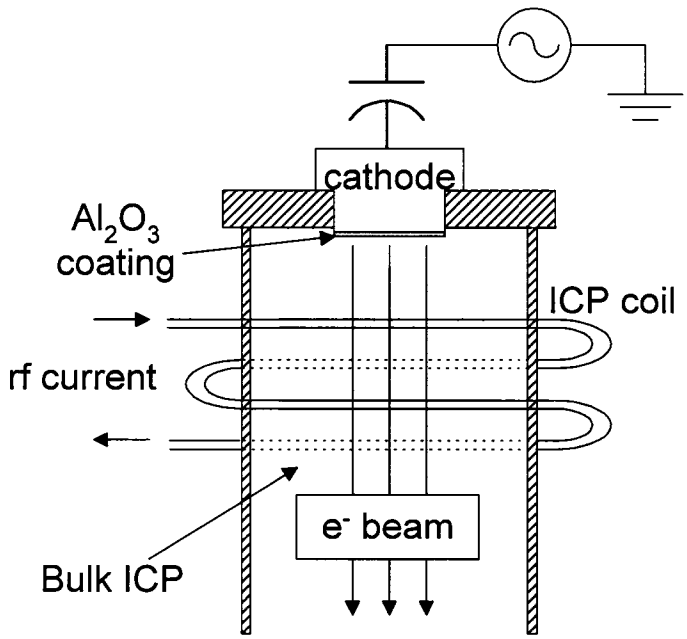

Figure 1.1 Schematic layout of the new rf biased DC electron beam source developed herein. Details of the system will be described in Chapter 2.

Pure capacitively coupled γ-mode rf discharges typically operate at 1 to 100 Torr, where electron-neutral collisions soon rob the energy of the

secondary electron, preventing electron beam transmission through the bulk plasma. The low pressure plasma provided by the ICP allows the transmission of accelerated secondary electrons emitted from the rf biased cold cathode over the longer mean free path available for energetic electrons at low pressures. Thus, an electron beam is created that can impinge on remote substrates for possible materials processing applications. Since the ICP power sets the electron beam current via the bulk plasma ion density, the cathode rf bias is primarily employed to set the sheath potential, which in turn sets the electron beam energy. This dual rf power source approach allows more independent control of the electron current and energy in the electron beam energy spectra as shown In Chapter 3 and modeled in Chapter 4.

1.2 Organization of Dissertation

In Chapter 2, a qualitative description of the operation of the electron beam source is given. Chapter 3 describes the experimental setup required to achieve the rf-driven DC electron beam and the diagnostic tools utilized in the experiments, and presents the experimentally measured electron beam energy spectra. In Chapter 4, a simple electron beam energy spectra model, based on an oscillating, collisionless Child-Langmuir sheath model is developed to explain the measured electron beam energy spectra. Chapter 5 describes the initial application of the electron beam to neutralize charge build-up and enhance pattern transfer during plasma oxide etching, and presents rudimentary modeling to verify how the electron beam enhances pattern transfer during oxide etch. Chapter 6 summarizes the present work and

speculates on potential applications of this source, its potential for wide area scalability, and the possible direction for future work on better understanding the physical foundations of the new electron beam source.

Chapter 1 References

[1)] Z. Yu, C. A. Moore, and G. J. Collins: IEEE J. Plasma Sci. **18** 753 (1990). See also J. Krishnaswamy and G. J. Collins: U. S. Patent 4,904,866 (1990).

[2)] B. Shi, Z. Yu, J. Meyer, and G. J. Collins: IEEE J. Plasma Sci. **14** 523 (1986).

[3)] J. D. Cobine: *Gaseous Conductors Theory and Engineering Applications* (Dover, New York, 1958).

[4)] G. Auday, Ph. Guillot, J. Caly, and H. Brunet: J. Appl. Phys. **83** 5917 (1998).

[5)] M. A. Lieberman and A. J. Lichtenberg: *Principles of Plasma Discharges and Materials Processing* (Wiley, New York, 1994).

[6] V. A. Godyak and A. S. Khanneh: IEEE Trans. Plasma Sci. **14** 112 (1986).

[7] P.P. Vitruk, R.J. Morley, H.J. Baker and D.R. Hall, Appl. Phys. Lett. **67**, 1366 (1995).

[8] P.P. Vitruk, R.J. Morley, H.J. Baker and D.R. Hall, Appl. Phys. Lett. **67**, 1366 (1995).

CHAPTER 2

QUALITATIVE DESCRIPTION OF PLASMA ELECTRON BEAM OPERATION

2.1 Ion-induced secondary electron emission

Secondary electron emission from surfaces under ion bombardment is a well-known process. Secondary emission is a result of the requirement of energy conservation when an ion recombines with an electron at a surface as shown in Figure 2.1 (reference 1). When an ion and an electron recombine, the electron [$e^-(1)$ in Figure 2.1] loses energy corresponding to the potential of the ion (the ionization potential). In order for the net energy of the reaction to balance, another electron inside the surface (termed $e^-(2)$ in Figure 2.1) must gain the amount of energy that the initial electron [$e^-(1)$] lost. If the energy gain of $e^-(1)$ is greater than the work function E_ϕ of the material, the electron escapes from the surface as a secondary electron. However, in a metal electrons are abundant in the conduction band, allowing rapid collisional thermalization of electron $e^-(2)$ When the energy is shared among many electrons, the probability that any electron will gain enough energy to surmount the work function is generally low. Thus, metals often make poor secondary electron emitters. On the other hand, in an electrically insulating material with few electrons available in the conduction band, secondary electron emission is more likely.

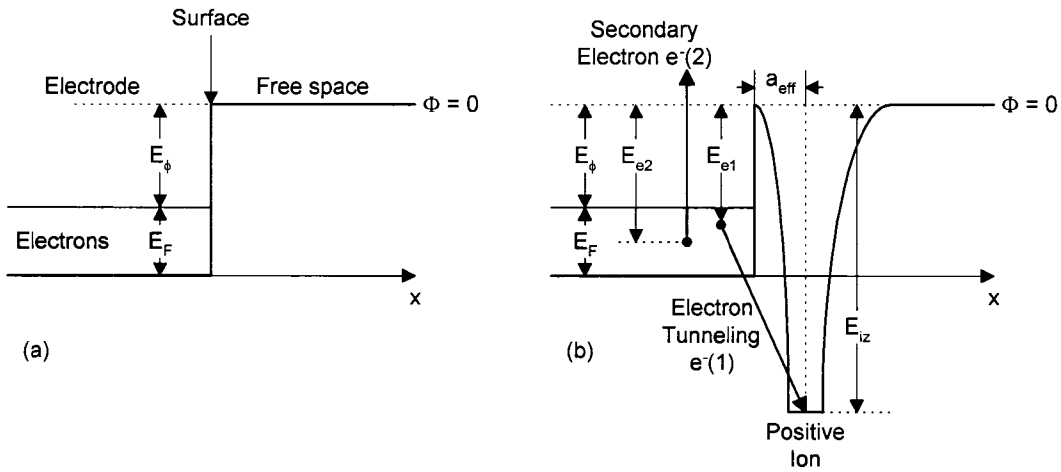

Figure 2.1 Energy diagrams for the ion-induced secondary electron emission process. (a) shows the work function of the electrode E_ϕ, which is the energy an electron must gain to escape surface. (b) shows electron-ion recombination near the surface, which for conservation on energy requires electron $e^-(2)$ to gain energy corresponding to the energy lost by $e^-(1)$ in the recombination process. If the energy gain by $e^-(2)$ is greater than the work function, the electron escapes the surface as an emitted secondary electron. From M. A. Lieberman and A. J. Lichtenberg: *Principles of Plasma Discharges and Materials Processing* (Wiley, New York, 1994).

2.2 Secondary electron emission from DC biased cold cathodes

Typically, secondary electron emission is produced by placing a conducting surface, to which a negative bias voltage is applied, in contact with a plasma[1,2] as shown in Figure 2.2. The negative bias tends to repel electrons from a region of the plasma adjacent to the electrode, forming a region of positive space charge known as a "sheath". Positive ions are accelerated through the sheath, gaining energy and impinging on the electrode surface, causing secondary electron emission. The same sheath that accelerates ions into the electrode tends to accelerate the emitted electrons from the electrode surface and back into the plasma. Under appropriate plasma and electrode configurations, the emitted secondary electrons may be formed into an electron

beam, which then propagates through the plasma to a remote location. However, since conducting materials must be used when applying DC bias to the electrode, high efficiency secondary electron beams using DC power are difficult to achieve, unless the cathode is formed from fragile and expensive cermet material. Herein, in order to utilize high secondary electron emission insulating cathode materials, we apply radio frequency bias to the electrode to form an electron beam.

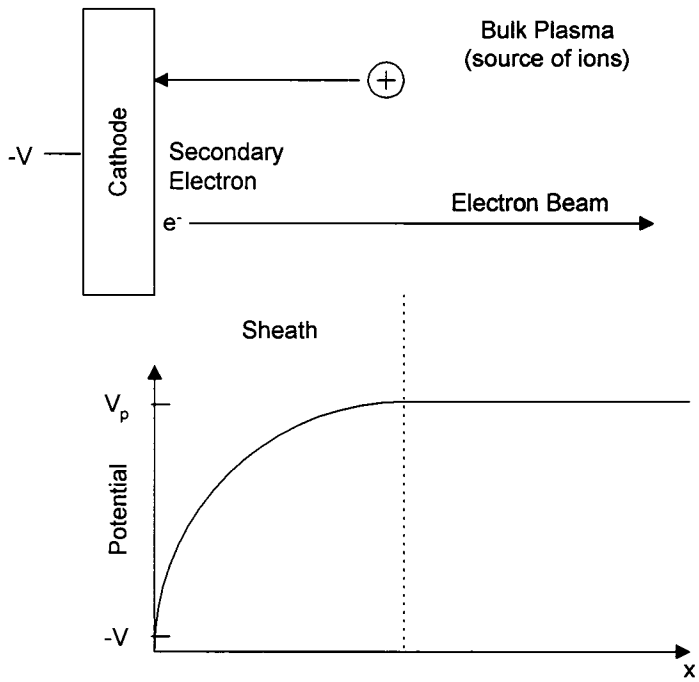

Figure 2.2 Schematic diagram of the secondary electron emission process from a negatively DC biased electrode (cathode) placed in contact with a plasma. The negative potential on the cathode surface accelerates ions from the plasma, which cause secondary electron emission upon impact. The secondary electrons are then accelerated back into the plasma by the sheath potential, forming a beam.

2.3 Secondary electron emission from rf biased plasma electrodes

In contrast to the DC biased electrode case, secondary electron emission from rf biased plasma electrodes is a known but generally neglected

phenomena.[3] On nearly all types of rf biased electrodes, a net DC bias is created as the result of the large mass difference between electrons and ions ($M_+ / m_e \sim 10^5$) and the requirement of zero net current to the electrode[1]. Figure 2.3 schematically illustrates the ion bombardment and secondary electron emission process driven by the sheath potential that occurs at the surface of a planar rf electrode with a DC self bias. Figure 2.3 also indicates the maximum and minimum sheath potentials and spatial locations as well as the rf sheath oscillation region which creates the effective DC sheath potential. Ions are accelerated toward the electrode by the effective DC sheath produced by the applied rf bias. When an ion impacts the electrode with incident energy E, $\gamma(E)$ secondary electrons are released from the surface (where $\gamma(E)$ is the number of emitted electrons per incident ion, as a function of incident ion energy). The sheath potential accelerates the emitted secondary electrons away from the electrode and into the bulk plasma, where an electron beam may be formed under appropriate conditions. As will be discussed in Chapter 3, the beam has an energy spectrum that depends in a complex way on the sheath voltage waveform, ion energy distribution impinging on the electrode, secondary electron emission coefficient of the cathode, and electron-neutral collisions experienced by electrons during propagation through the bulk plasma.

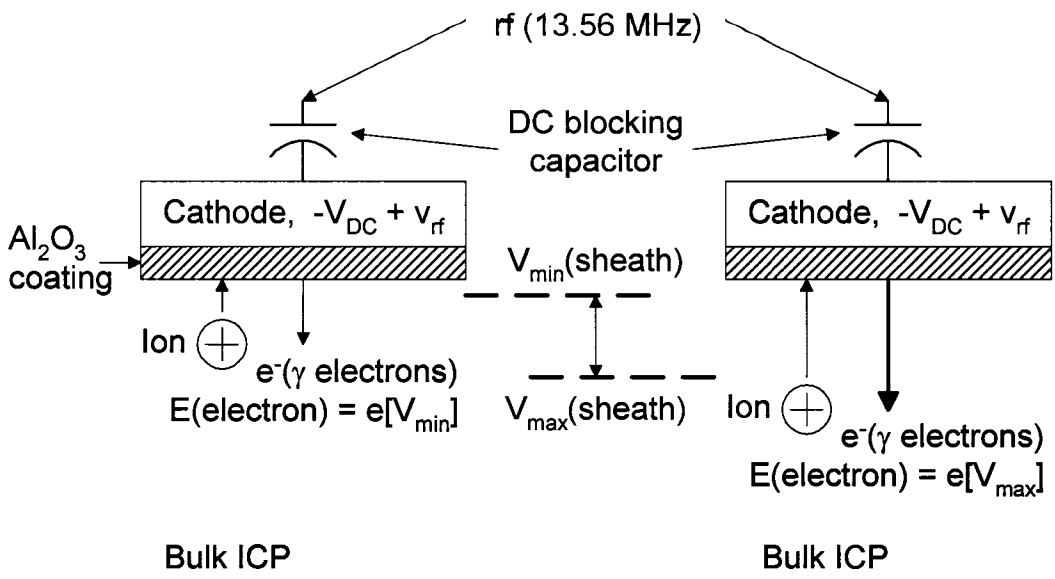

Figure 2.3 Sketch of the electron beam formation at the most positive (V_{min}) and most negative (V_{max}) portion of the cathode rf bias voltage cycle. The net DC bias on the Al_2O_3 cathode surface attracts ions from the bulk ICP, and the instantaneous rf + DC potential accelerated emitted secondary electrons from the cathode into a beam.

By taking advantage of the ability of rf current to be capacitively coupled through electrically insulating surfaces, the relatively high secondary electron emission coefficient of Al_2O_3 may be utilized to create high efficiency cathode surfaces in plasmas. Employing proper plasma conditions and cathode design will allow the formation of high efficiency electron beams, as discussed in detail in Chapter 3.

Chapter 2 References

[1] M. A. Lieberman and A. J. Lichtenberg: *Principles of Plasma Discharges and Materials Processing* (Wiley, New York, 1994).

[2] J. D. Cobine: *Gaseous Conductors Theory and Engineering Applications* (Dover, New York, 1958).

[3] X. Meng, Y.-N. Wang, and T.-C. Ma, J. Appl. Phys. **88**, 40 (2000).

CHAPTER 3

EXPERIMENTAL SETUP AND DIAGNOSTIC TOOLS

Chapter 3 covers the experimental details of the plasma electron beam generation. Additionally, the diagnostic tools used to characterize the plasma and the electron beam are described. Finally, the measured electron beam energy spectra over a wide range of ICP and cathode bias conditions are presented.

3.1 Experimental setup

The experimental plasma generated electron beam source is composed of two main parts: the inductively coupled plasma generation section and the cathode section, as shown in Figure 3.1. Traditional capacitively coupled discharges operate most efficiently at pressures above 100 mTorr, where the electron mean free path is typically of the order of centimeters or less. Any electron beam produced in such conditions will soon be robbed of its energy by collisions with background gas atoms or molecules. By adding separate control of the plasma generation via the ICP, the operating pressure is reduced to the 1 – 20 mTorr range where the electron mean free path is increased to 10's of cm, allowing efficient, essentially collision-free electron beam propagation.[1] The design considerations of the ICP portion of the electron beam source are described in detail in section 3.1.1. In section 3.1.2, the cathode design and rf

bias details are covered, while in section 3.1.3, the tools used to characterize the plasma and the electron beam are presented.

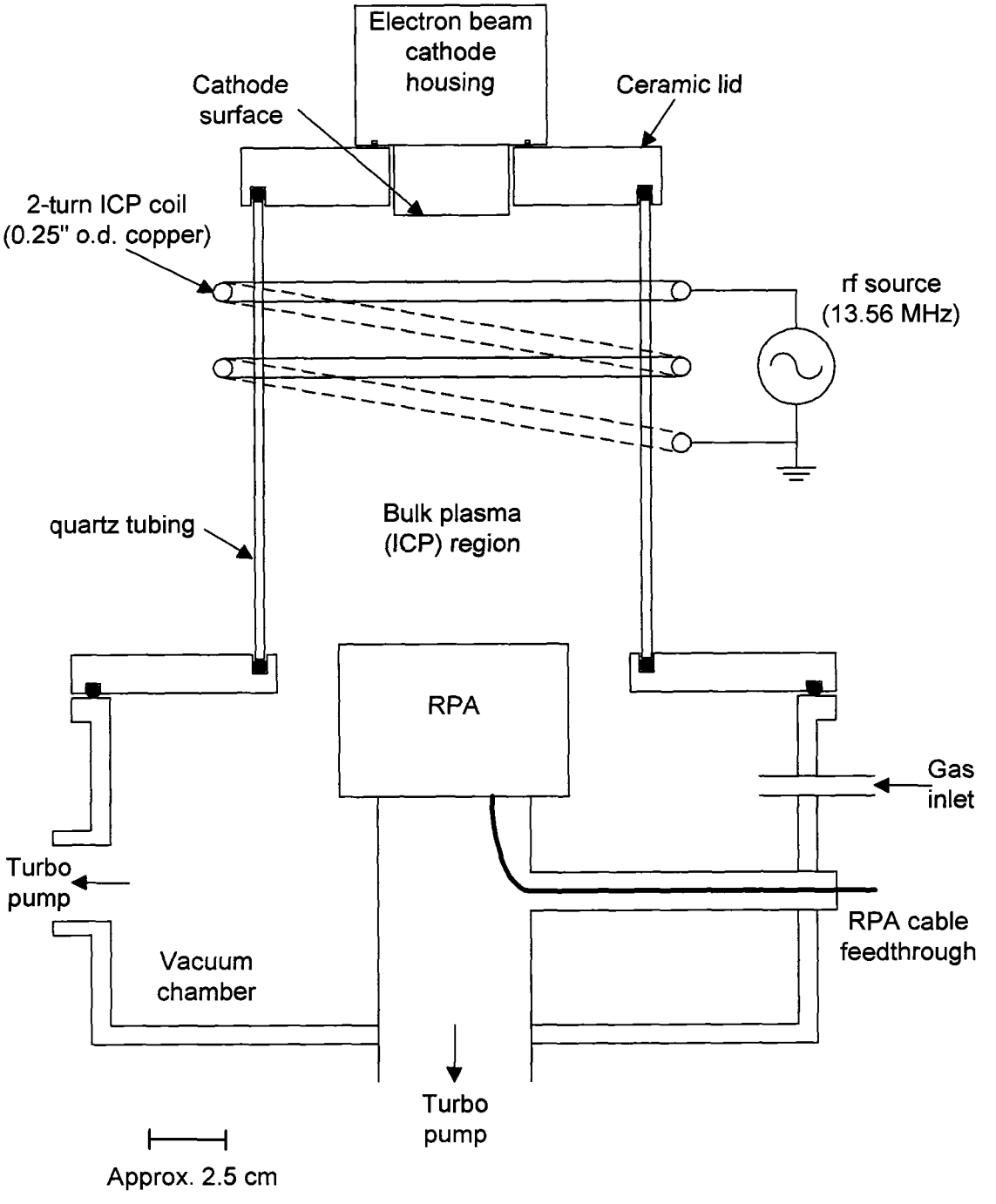

Figure 3.1 Schematic diagram of the experimental electron beam generation apparatus.

3.1.1 ICP generation

The inductively coupled plasma is sustained by rf current (13.56 MHz herein) passing through the two-turn copper coil wound around a 10 cm o.d. quartz cylinder with one open end on the bottom. The top closed end of the cylinder contains the cold cathode (covered in section 3.1.2), and the open bottom contains the retarding potential analyzer used to measure the electron beam energy spectra (see section 3.1.3). Power to the ICP coil is typically varied from 125 to 500 W as controlled by the rf power supply (Advanced Energy RFG 1250). A standard "L"-type match network, constructed at CSU and shown schematically in Figure 3.2, transforms the inductive impedance of the ICP to the 50 Ω impedance of the rf power supply. Variable vacuum capacitors allow the match network to be adjusted to a wide range of plasma impedances. An internal directional coupler power measurement circuit on the output section of the rf power supply measures the power delivered to the match network/plasma circuit. No reflected power is recorded over the entire range of experimental conditions; i.e. a 50 Ω match is always achieved. The calibration of the power measurement circuit was measured independently using a separate 50 Ω directional coupler placed in the coaxial transmission line between the power supply and the match network. In all experimental data presented, the ICP power is taken to be the generator output power. Thus, any power losses in the match network, as well as resistive power losses in the ICP excitation coil, are ignored. Based on prior experimental work, the maximum total error introduced

by neglecting parasitic power losses is expected to be less than 20%, and run – to – run errors are expected to be in the 10 % range.[2]

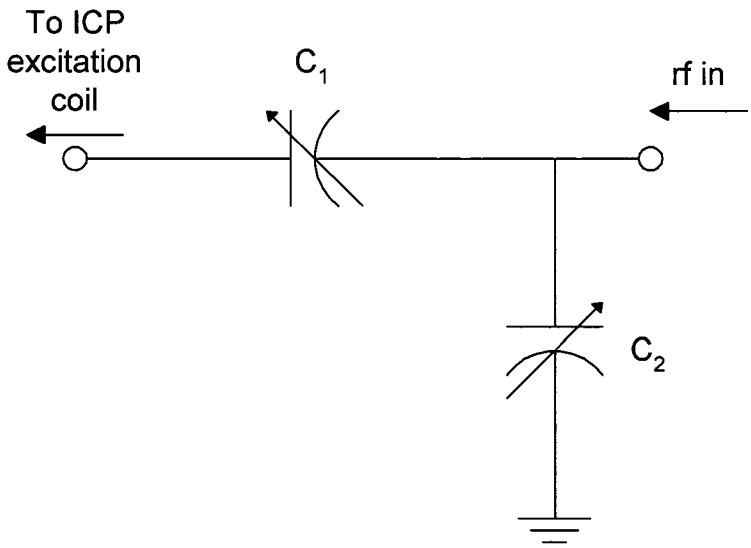

Figure 3.2 Standard "L" type match network used to transform the inductive load of the ICP system to the 50 Ω impedance of the rf power supply. Capacitors C_1 and C_2 are variable vacuum capacitors designed for low power loss in high power rf applications. The match network is housed in a grounded aluminum box for safety and to reduce broadcast rf noise.

Inductively coupled plasma feedstock gas pressure is varied from 2 to 20 mTorr by changing the gas flow into the chamber using standard mass flow controllers (MKS 1159A). Chamber pressure is measured using a capacitance manometer (MKS Baratron, 1 Torr range). The capacitance manometer is zeroed at the beginning of each experiment by pumping the chamber to its base pressure with a turbomolecular pump [p(base) < 10^{-6} Torr, verified by ionization gauge]. Additionally, the capacitance manometer was factory calibrated at the beginning of the experimental work described herein. For a given gas flow into the chamber, a constant chamber pressure was measured over the course of the

experiments. Thus, it is speculated that the pressure data used herein is accurate and repeatable to within the 3% specification of the capacitance manometer.

3.1.2 Cathode construction and biasing

The details of the cold cathode and cathode housing are shown in Figure 3.3. The electron beam is intended to operate for long periods of time (hours) in a relatively high power density plasma environment. Viton rubber o-rings are used to form the required vacuum seals, and Viton has a maximum operating temperature of 200 °C. Thus, the cathode housing is designed to be water-cooled. The primary motivation for water-cooling was to keep the o-ring seals well below their maximum operating temperature. A second motivation for water-cooling was to try and maintain the cathode surface at a constant temperature to ensure constant secondary electron emission over time. It is uncertain if this step was necessary, but it helped to reduce the number of experimental variables.

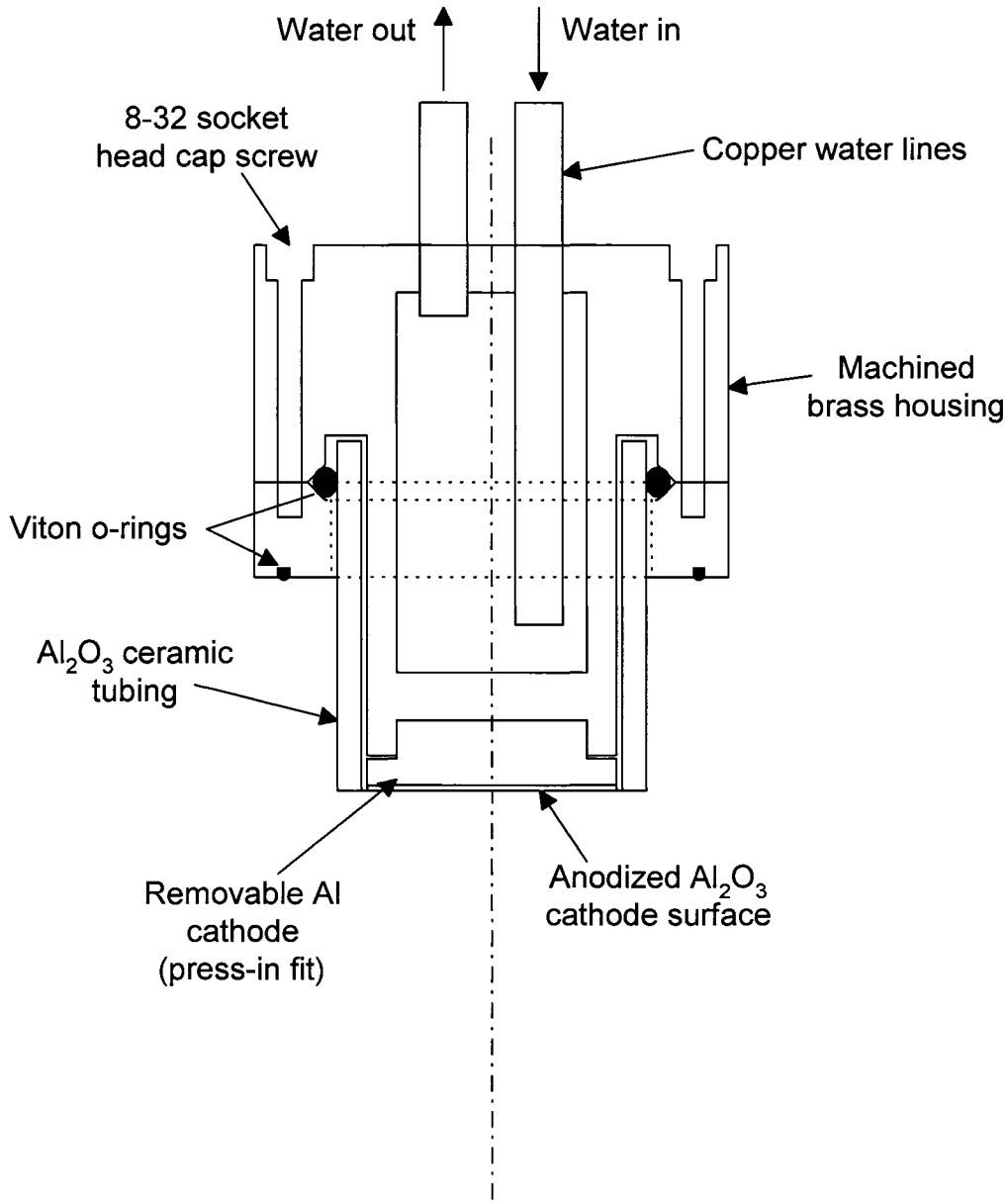

Figure 3.3 Schematic of the rf biased cathode housing.

The alumina ceramic tubing surrounding the cathode was used to keep only the face of the cathode in contact with the plasma. The intention of this design was to minimize the sputtering of anodization at the sharp cathode edge, where the electric field is highest. Some preferential sputtering was noted at the edges after ~ 10 hours of operation, but was later minimized by rounding the

cathode edges (radius ~ 1 mm) before anodization. With the edge rounding and ceramic tube in place, cathode lifetime was approximately 30 – 100 hours, depending on plasma conditions.

Radio frequency voltage (generally 13.56 MHz), typically from 280 to 850 V (peak to peak), is applied to the cathode housing. Cathode rf potential is monitored using a high voltage oscilloscope probe. A 125 μm thick anodized aluminum (Al_2O_3) coating, such as employed in rf plasma etch chamber electrodes, is applied to the aluminum cathode as shown in Figure 3.3. The cathode surface is exposed to the existing bulk ICP through the insulating top plate of the plasma reactor.

A match network was required to transform the capacitive impedance of the rf biased electrode to the 50 Ω impedance of the rf power supply (Advanced Energy RFG1250). Figure 3.4 shows the circuit diagram of the match network. Details of match network design and construction are available in the M.S. Thesis of L. Knipp of CSU[3]. In contrast to the higher power transmission requirements of the ICP match network, which required vacuum variable capacitors, the relatively low power consumption of the rf cathode allowed use of low cost air dielectric variable capacitors. Due to the large mass difference between electrons and ions, a net negative DC bias voltage of $V_{DC} \approx \frac{1}{2}v_{rf}$(peak to peak) forms across the plasma sheath between the insulating cathode surface, which acts as a DC blocking capacitor, and the bulk plasma.[4] This effective DC sheath voltage is responsible for both attracting the positive ions to the cold cathode surface and accelerating the secondary electrons away from the

surface, forming the plasma generated electron beam. In addition to the "natural" capacitance of the insulating cathode surface, an additional "blocking" capacitor was added in series with the electrode, on the output side of the match network. The purpose of the blocking capacitor is to protect the variable air capacitors and the power supply from any DC voltage developed during beam operation. For example, in the event of any pinhole formation or erosion of the anodization, the DC bias voltage developed on the electrode surface will be shorted directly to the air dielectric capacitors in the match network. Air core variable capacitors are designed for a fairly low DC operating voltage, and the additional DC voltage could be enough to arc the match network.

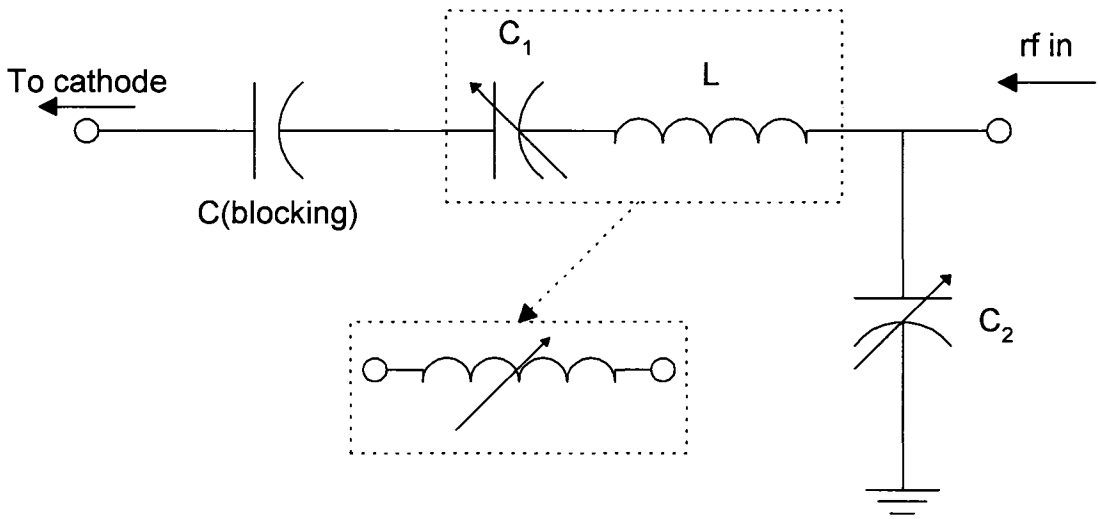

Figure 3.4 Circuit diagram of the rf-biased cathode match network. The large (3 nF) DC blocking capacitor is included. Notice that the C_1 + L series combination is used as a variable inductor. By varying C_1 and C_2, the entire range of cathode impedances could be transformed to the 50 Ω impedance of the rf power supply. The entire circuit is housed in a grounded aluminum box approximately 25 x 30 x 15 cm.

3.1.3 Diagnostic instruments

3.1.3.1 Retarding Potential Analyzer for Electron Beam Energy Spectra Measurements

In order to gain quantitative information about the electron beam formed at the capacitively biased electrode and transmitted through the ICP, a retarding potential analyzer (RPA) is utilized. Retarding potential analyzers have been used extensively to measure both ion and electron energy spectra incident on grounded and biased surfaces in plasma reactors. Ion beam energy spectra are also commonly measured with RPA's.

The basic operating principle of RPA's is to use various biased grids to repel unwanted charged species (ions in this work) and allow passage of the species of interest (electrons herein). The bias voltage on one of the grids may be varied in order to allow passage of selected species only within a certain energy range. Figure 3.5 sketches the general theory of operation of RPA's used for electron energy spectra measurement.

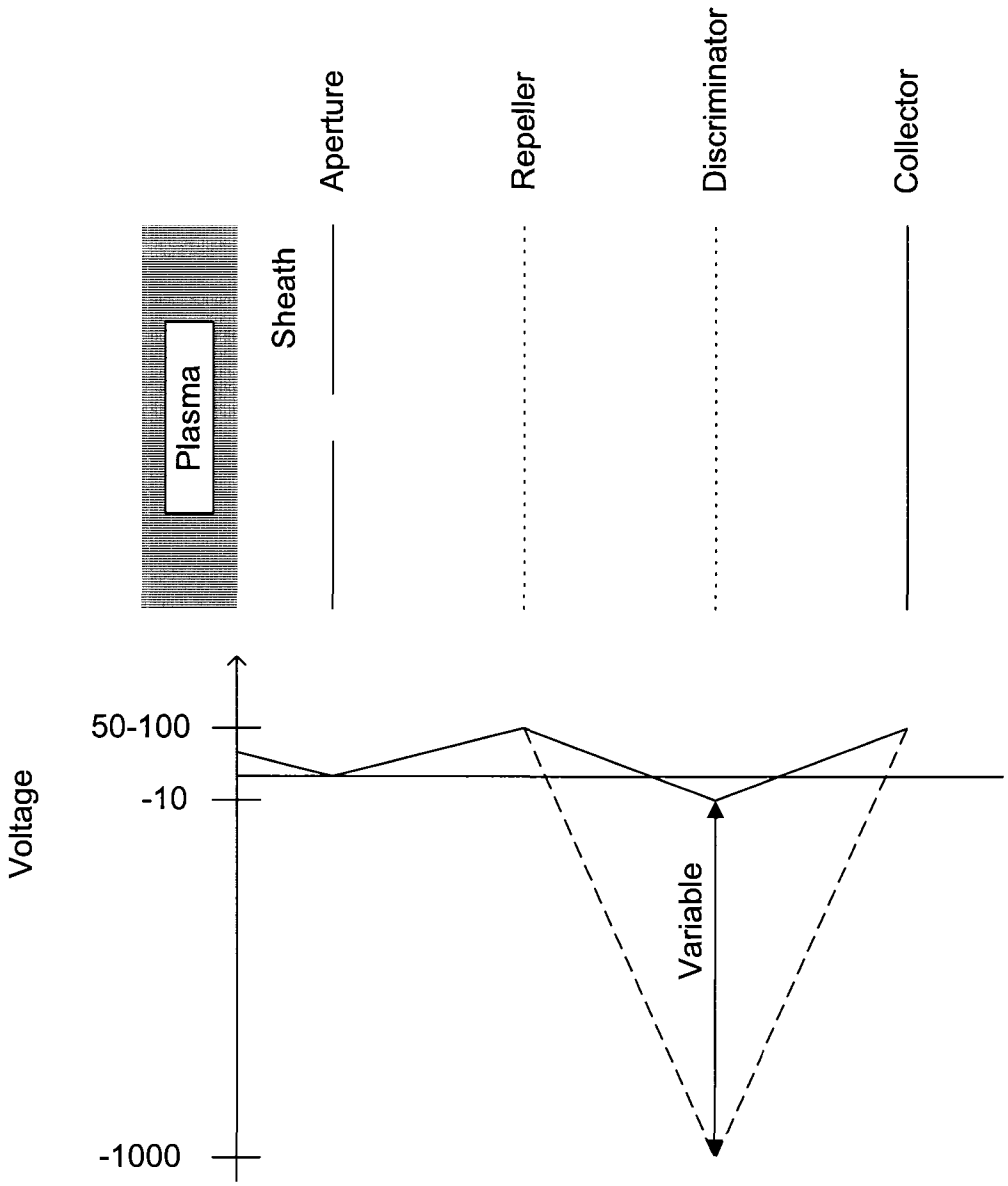

Figure 3.5 Electric potentials on the various grids in a retarding potential analyzer used for electron beam energy spectra measurements. For ion energy measurements, the polarity of the applied voltages is reversed.

To avoid collisions between the charged species of interest and background gases in the RPA, two general designs are typically utilized. The first RPA design seeks to minimize the distance between the biased grids, such that the grid spacing is much less than the mean free path of the species of interest. This design is easy to implement, but at the expense of several potential problems. First, since these devices are very compact, heat dissipation is often a difficult issue to overcome. Second, proper electrical isolation of the grids may be difficult, since grid spacing may be less than 1 mm. Finally, if the gas pressure and electric fields are at appropriate levels within the RPA, secondary plasma discharges may occur within the device, resulting in erroneous data.

The second type of RPA design, utilized herein, is differentially pumped. That is, the spatial volume containing the biased grids is maintained at vacuum conditions (i.e. low enough pressure) to keep the charged particle mean free path much greater than the grid spacing. Due to the requirement of additional vacuum pump systems, the experimental implementation of such a design is more difficult than non-differentially pumped designs, but most of the practical issues presented by RPA operation in low vacuum conditions are eliminated. For example, heat dissipation issues are generally reduced due to the larger size of grids and fixtures, and grid spacing may be as large as 10's of millimeters, making electrical isolation of grids straightforward. Finally, at the vacuum conditions inside of differentially pumped RPA's (typically 10^{-5} – 10^{-6} Torr), the possibility of secondary discharges is virtually eliminated.

Herein, a differentially pumped retarding potential analyzer (RPA) is placed 14 cm below the center of the cold cathode to measure the transmitted electron beam energy spectra. The beam is sampled through an electrically grounded 200 μm diameter aperture in a 100 μm thick brass plate. Ambient pressure in the RPA is maintained below 10^{-5} Torr using a turbomolecular pump, as monitored with an ionization gauge, to minimize gas phase collisions between beam electrons and background gas in the RPA, which could introduce errors in the measured beam energy spectra.

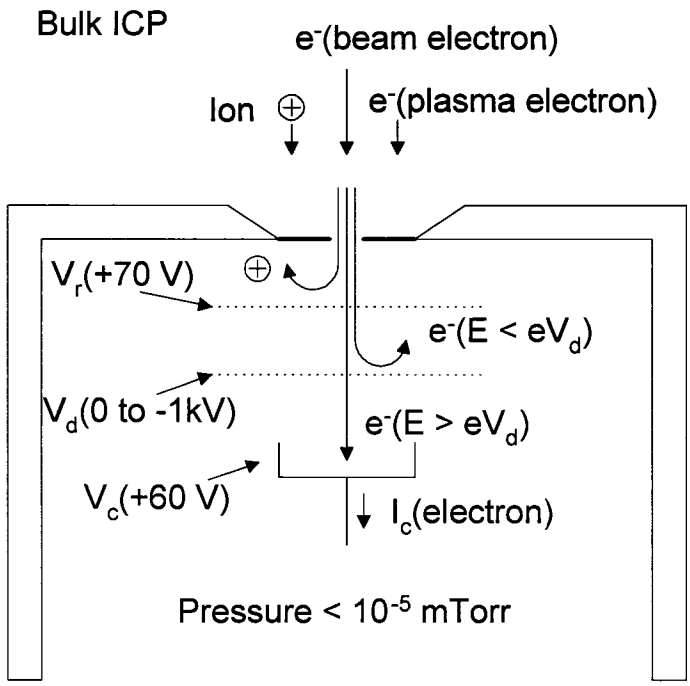

Figure 3.6 Sketch of the retarding potential analyzer (RPA) used to measure the electron beam energy spectra. The RPA housing is electrically grounded to the chamber ground and is constructed of stainless steel. The aperture is 200 μm diameter in 100 μm thick brass. Typical grid and electrode bias voltages are shown. Electrical ground is referenced to the housing and aperture, which are in good electrical contact with the chamber ground.

The RPA consists of two grids, the ion repeller grid and the electron energy discriminator grid, and Faraday cup electron collector. The ion repeller and electron energy discriminator grids are made of 304 stainless steel mesh (100 lines/cm, transmission T = [open area]/[total area] ~ 35 %). Dimensions of the RPA are 2.4 mm between the grounded orifice and the ion repeller grid, 9.5 mm between the ion repeller grid and the electron energy discriminator grid, and 0.8 mm between the electron energy discriminator grid and the opening in the Faraday cup electron collector. Both the ion repeller grid and the Faraday cup electron collector are negatively biased (~ - 60 V). The potential of the discriminator grid is swept from 0 to +1000 V and current on the collector electrode is measured. The electron energy distribution is calculated from the derivative of the I_c - V_d plot, in standard fashion.[5] The resolution of the RPA is estimated to be approximately 10 - 20 eV in our experimental conditions.[6]

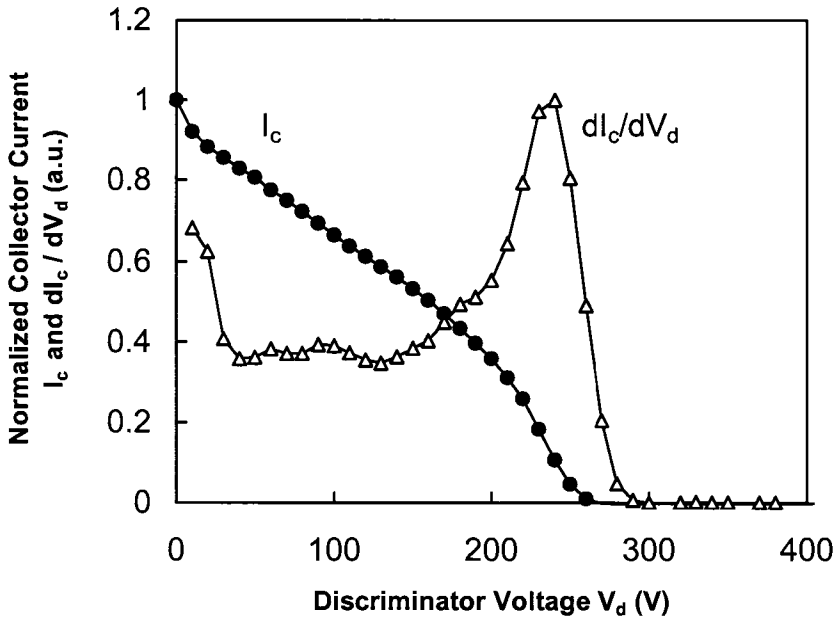

Figure 3.7 Sample electron beam collector current (I_c) – discriminator voltage (V_d) plot taken using the retarding potential analyzer (RPA) and the first derivative dI_c/dV_d, which represents the electron beam energy spectra. Plasma/electron beam conditions are P_{icp} = 250 W, p_{Ar} = 2 mTorr, and $V_{cathode}$ = 280 V_{p-p}.

3.1.2 Langmuir Probe for Bulk Inductively Coupled Plasma Electron Density and Temperature Measurements

Plasma electron density n_e and electron temperature T_e are independently measured with a rf compensated Langmuir Probe. Orbital motion limited (OML) theory is used for the plasma electron density calculations.[5,7,8] The plasma electron temperature is derived from the relation: $V_p - V_f = (T_e / 2)\ln(M / 2\pi m) + T_e / 2 \approx 5.2T_e$ for argon,[5] where V_p is the plasma potential (Volts), V_f is the floating potential (Volts), M is the argon mass ($40 \times 1.67 \times 10^{-27} = 6.64 \times 10^{-26}$ kg) and m is the electron mass (9.11×10^{-31} kg). Details on both the design of the

Langmuir probe used herein, as well as the OML probe theory, are covered in detail elsewhere (D. Shaw MS thesis).

In Figures 3.8 and 3.9, Langmuir probe data (n_e and T_e, respectively) are shown as measured over the experimental range of ICP rf power (125 –500 W) and argon gas pressure (2 – 20 mTorr) with the cathode bias off. Langmuir probe data is used in modeling the measured electron beam energy spectra (Chapter 4).

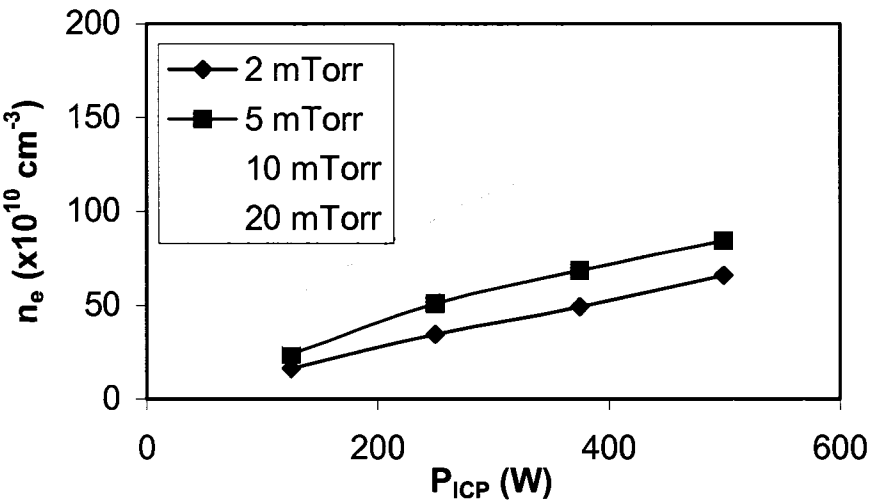

Figure 3.8 Plasma electron density n_e versus ICP power as measured using the Langmuir probe over the argon pressure range of 2 – 20 mTorr. The measured n_e data is used in modeling the electron beam energy spectra in Chapter 4.

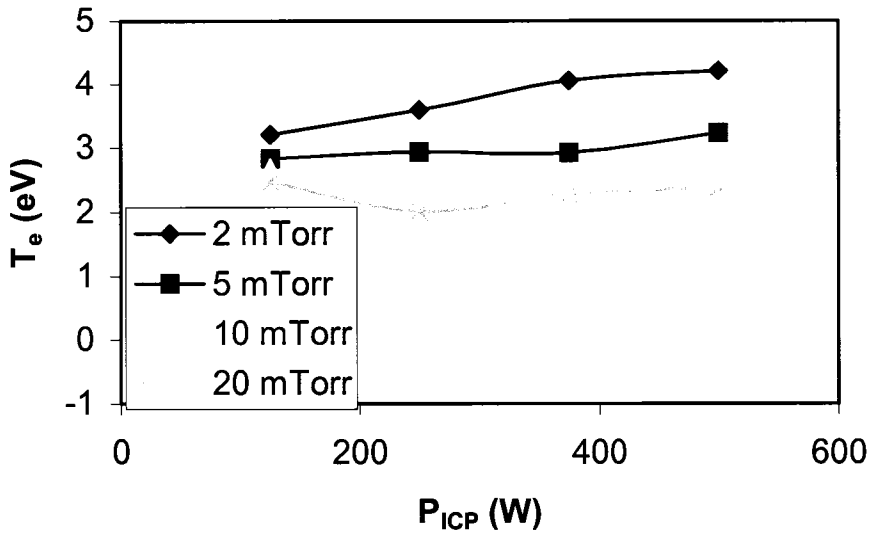

Figure 3.9 Plasma electron temperature T_e versus ICP power as measured using the Langmuir probe over the argon pressure range of 2 – 20 mTorr. The measured T_e data is used in modeling the electron beam energy spectra in Chapter 4.

In order to investigate the effect the cathode bias had on the bulk inductive plasma, the electron density was measured with the electron beam on. The axis of the Langmuir probe was kept parallel to the electron beam in order to minimize the effect of the beam electrons on the measured plasma electron density. Figure 3.10 shows the measured plasma electron density over the 0 – 850 V(peak-to-peak) cathode bias range for 2 mTorr argon. Other argon gas pressure data was similar. Deviation in measured n_e is less than 10 % over the entire cathode bias voltage range, which is less than the expected 20 % accuracy of the Langmuir probe.

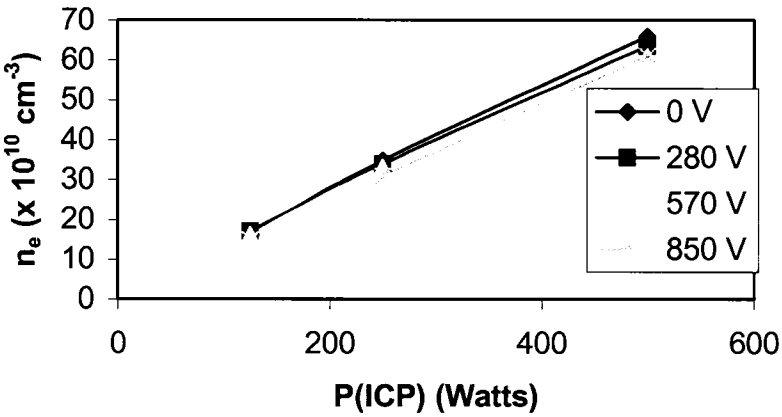

Figure 3.10 Measured plasma electron density at 2 mTorr argon gas pressure over the range of cathode bias voltages used experimentally. The maximum deviation between cathode-off and cathode-on conditions is less than 10 %.

The results of electron temperature measurements at 2 mTorr argon pressure with and without cathode bias are shown in Figure 3.11. Measured electron temperature varies by about 30 % over the range of cathode bias voltages. The reason for the wide range of measured T_e is uncertain, although increased rf plasma potential variations with increasing rf cathode bias voltage may have caused errors in measuring the plasma potential V_p, as discussed by Godyak et al., which is used to calculate T_e in the equation $V_p - V_f = (T_e / 2)\ln(M / 2\pi m) + T_e / 2 \approx 5.2T_e$. Although the Langmuir probe is rf compensated, meaning that rf plasma potential variations should not effect measured data, compensation may be less than perfect. Note that even a small perturbation in measured V_p can lead to a fairly large error in calculated T_e (e.g. 1 V error leads to $1 / 5.2 \approx 0.2$ eV error in T_e). Capacitive probe measurements of the rf plasma potential indicated an increase in rf plasma potential from a few volts peak without cathode bias to 10 – 20 V(peak) with cathode bias on, possibly verifying

the above speculation. Nevertheless, the model uses the square root of the measured T_e, minimizing any errors introduced to the model via T_e measurement errors.

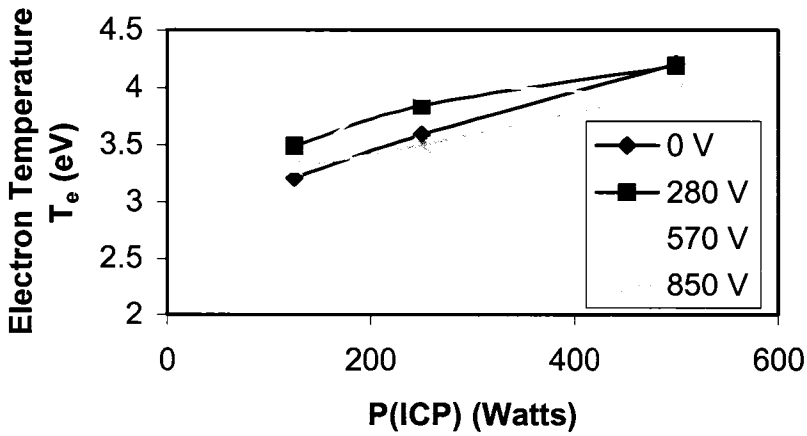

Figure 3.11 Measured plasma electron temperature at 2 mTorr argon gas pressure over the range of experimental cathode bias voltages.

3.2 Measured electron beam energy spectra results

3.2.1 Argon feedstock gas

Figures 3.12 – 3.15 show the measured electron beam energy spectra at a distance 14 cm from the cold cathode in 2 mTorr (Figure 3.12), 5 mTorr (Figure 3.13), 10 mTorr (Figure 3.14) and 20 mTorr (Figure3.15) argon feedstock gas. Three separate peak to peak rf voltages are applied to the cold cathode: 280, 570, and 850 V; and four ICP powers are used to excite the bulk plasma: 125, 250, 375, and 500 W. The ICP power referred to herein is the total power supplied by the rf generator to the rf coil. Coil resistive losses and match network losses are neglected.

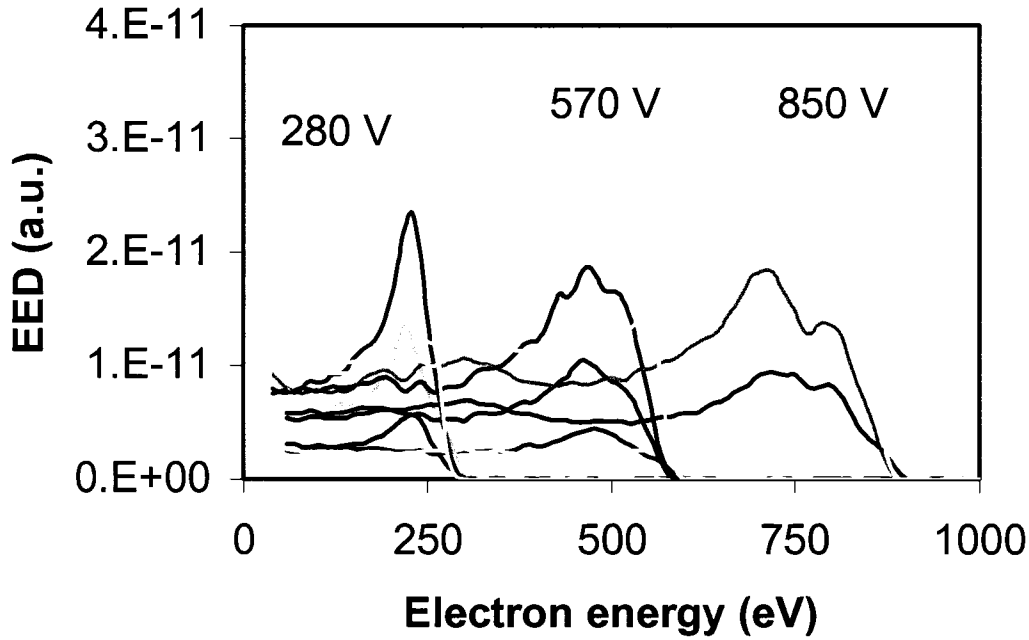

Figure 3.12 Measured electron beam energy spectra acquired with the retarding potential analyzer. ICP conditions are 2 mTorr Argon, 125 W, 250 W, 375 W and 500 W in order of increasing EED magnitude. Electrode rf bias voltages (in rf Volts, peak-to-peak) are shown.

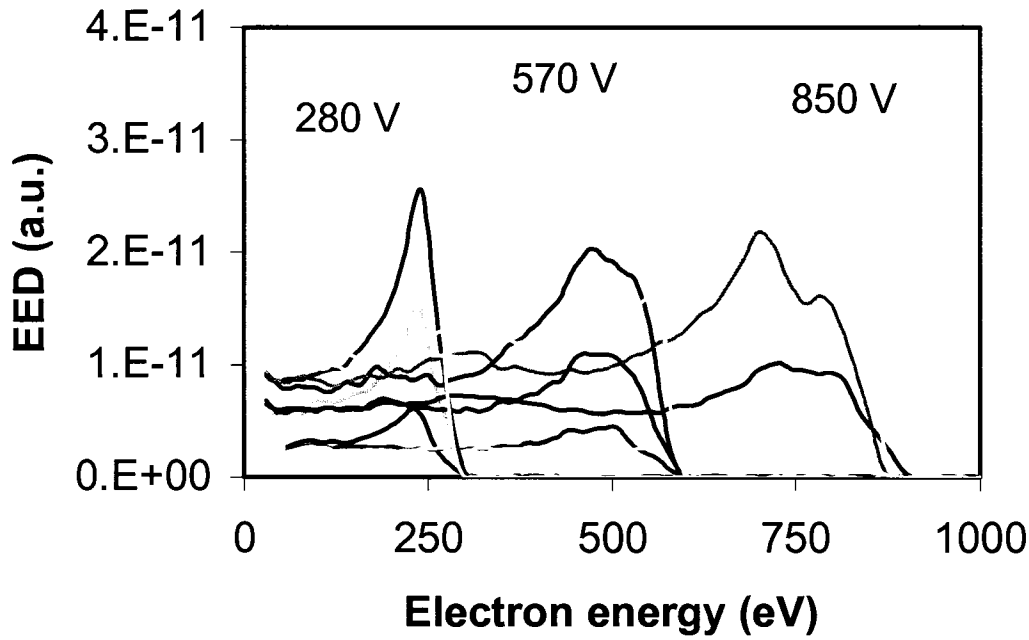

Figure 3.13 Measured electron beam energy spectra acquired with the retarding potential analyzer. ICP conditions are 5 mTorr Argon, 125 W, 250 W, 375 W and 500 W in order of increasing EED magnitude. Electrode rf bias voltages (in rf Volts, peak-to-peak) are shown.

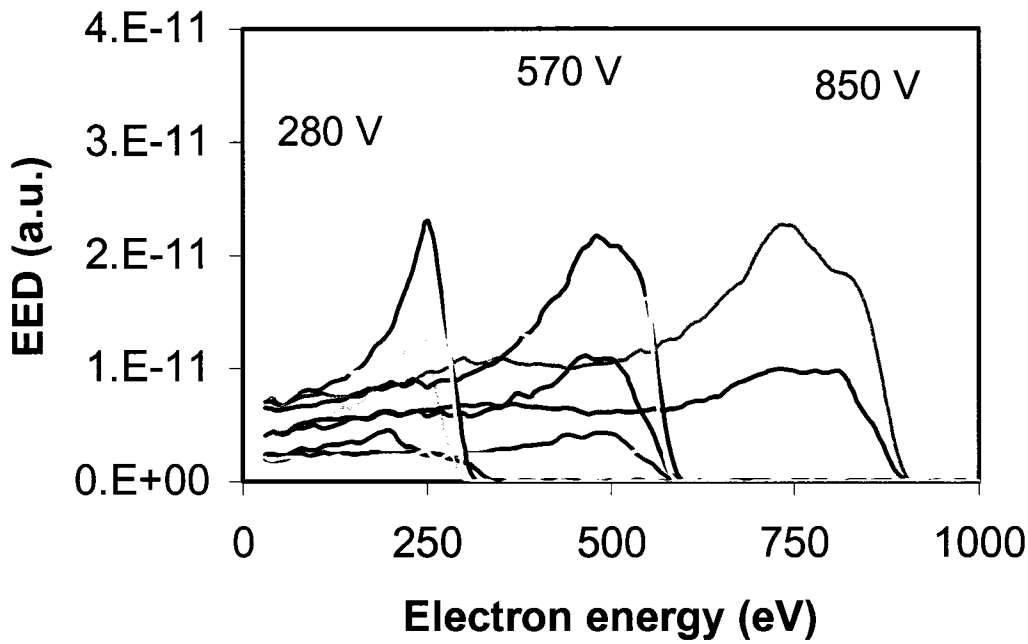

Figure 3.14 Measured electron beam energy spectra acquired with the retarding potential analyzer. ICP conditions are 10 mTorr Argon, 125 W, 250 W, 375 W and 500 W in order of increasing EED magnitude. Electrode rf bias voltages (in rf Volts, peak-to-peak) are shown.

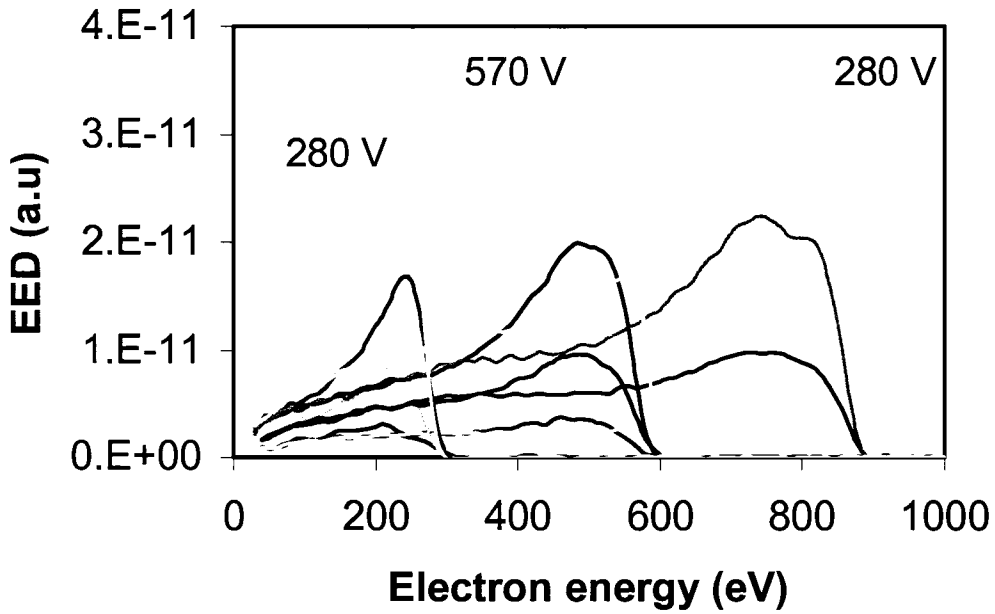

Figure 3.15 Measured electron beam energy spectra acquired with the retarding potential analyzer. ICP conditions are 20 mTorr Argon, 125 W, 250 W, 375 W and 500 W in order of increasing EED magnitude. Electrode rf bias voltages (in rf Volts, peak-to-peak) are shown.

Two important points are noted in Figures 3.12 – 3.15. First, the maximum electron beam energy measured by the RPA corresponds to the maximum peak to peak rf voltage applied to the cold cathode. This is the case for maximum beam energy observed over the entire ICP power and pressure range investigated herein, as shown in Fig. 3.16.

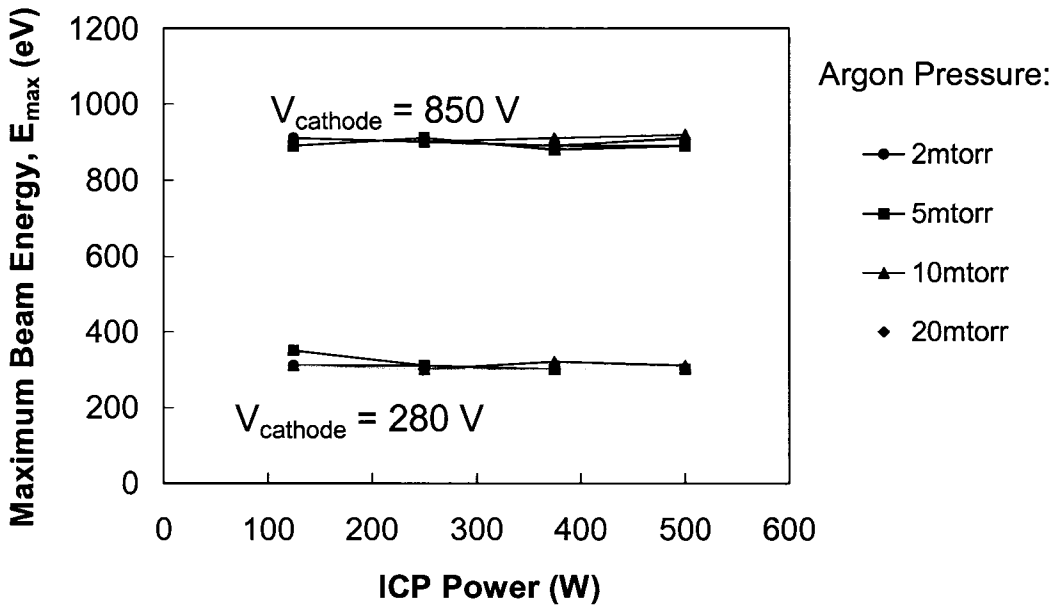

Figure 3.16 Maximum electron energy as a function of ICP power (related to ICP density). The beam energy peak is independent of ICP conditions and only depends on the peak-to-peak cathode rf bias voltage.

The second important feature of the data in Figures 3.12 – 3.15 is that the measured total electron beam current increases with increasing ICP power. Neglecting coil resistive power losses, the ICP ion density, and hence the ion flux to the electrode, is proportional to applied ICP power.[5)] The secondary electron current goes as $|I_{electron}| = \gamma|I_{ion}|$, so it is expected that the measured secondary electron current should increase with increasing ion current to the cathode. Figure 5 shows this monotonic trend over the entire range of ICP powers and gas pressures studied herein.

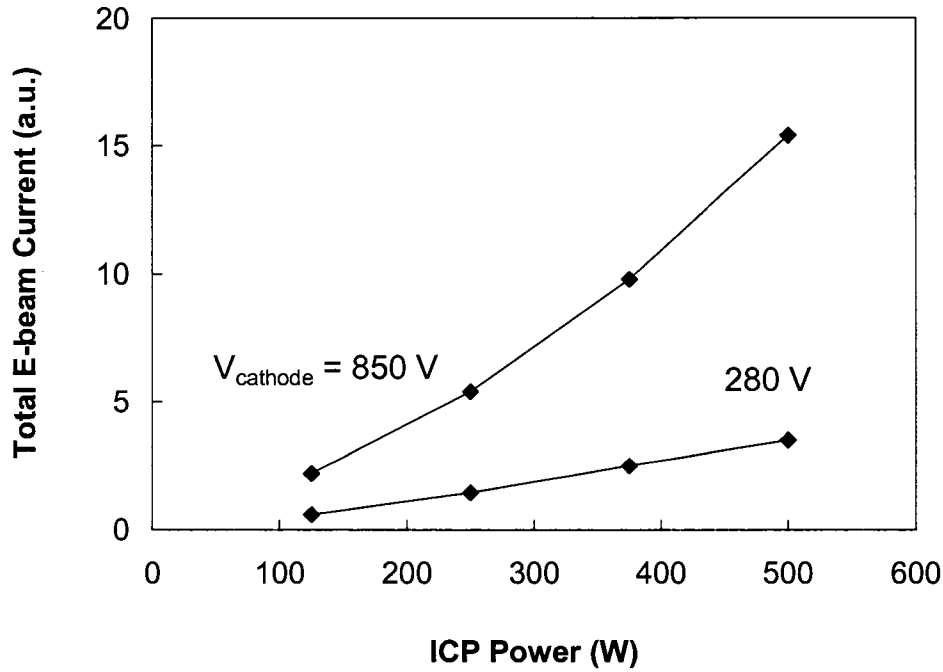

Figure 3.17 Total (i.e. integrated) electron beam current versus ICP power (which to first approximation is proportional to plasma ion density). Argon gas pressure is 2 mTorr for the data shown, but all pressures exhibit similar behavior.

This may indicate the absence of strong beam-plasma interactions under these experimental conditions. The data of Figures 3.16 and 3.17 may both indicate that no second order electron beam-plasma interactions are occurring under the experimental conditions utilized herein. For example, a reduction in measured electron current at higher pressures could indicate that electron-neutral collisions are scattering the beam as it passes through the ICP. However, as indicated in the data of Figures 3.12 – 3.15, the beam current increases with increasing pressure, following the increase in ion density, over the entire pressure range of 2 – 20 mTorr.

3.2.2 Hydrogen feedstock gas

In addition to the standard, well-understood argon feedstock gas of section 3.3.1, hydrogen gas was investigated briefly. Electron beam formation in a hydrogen ambient may be of some interest in materials processing applications such as deposition or post-deposition treatment of hydrogenated amorphous silicon (α-Si:H) films. Additionally, hydrogen feedstock provides a more complex plasma with two primary positive ion species (H^+ and H_2^+) to provide a more rigorous test of the electron beam energy spectra model developed in Chapter 4. The measured data is shown in Figures 3.18 and 3.19. Although not included herein, beam operation was successfully demonstrated in He, Ne, N_2, and O_2 feedstock gases as well.

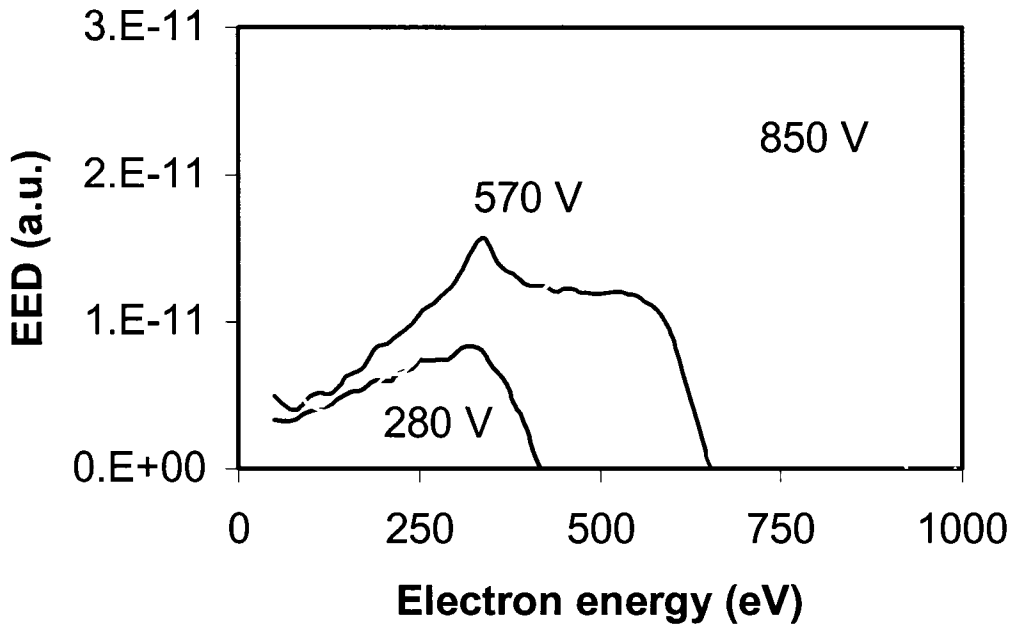

Figure 3.18 Measured electron beam energy spectra acquired with the retarding potential analyzer. ICP conditions are 20 mTorr H_2 and 250 W rf power. Electrode rf bias voltages (in rf Volts, peak-to-peak) are shown.

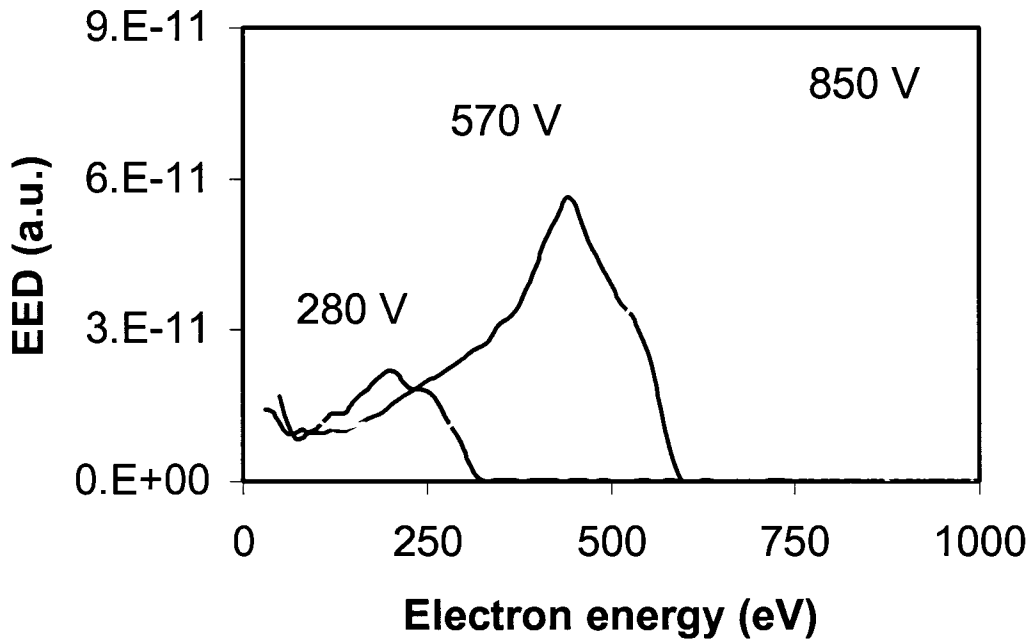

Figure 3.19 Measured electron beam energy spectra acquired with the retarding potential analyzer. ICP conditions are 20 mTorr H_2 and 500 W rf power. Electrode rf bias voltages (in rf Volts, peak-to-peak) are shown.

3.2.3 Oxide etch feedstock gas (CF_4)

Since the electron beam source will be applied to investigate its ability to reduce oxide etch non-idealities, electron beam energy spectra were recorded in oxide etch feedstock gas (CF_4) to confirm beam operation in etch conditions. Figure 3.20 shows the measured beam spectra, which confirm beam operation in oxide etch conditions. The principle difference between the CF_4 data shown in Figure 3.20 and other electron beam spectra data is that the rf bias frequency is 4 MHz, rather than the standard 13.56 MHz. The reduced frequency of 4 MHz is used in etching experiments discussed in Chapter 5 since the substrate bias frequency for etching is 13.56 MHz. No attempt will be made in Chapter 4 to

model the measured beam spectra in etch gas due to the complexity of the plasma. Nevertheless, the spectra of Figure 3.20 proves that electron beam generation and propagation occurs in CF_4 feedstock plasmas.

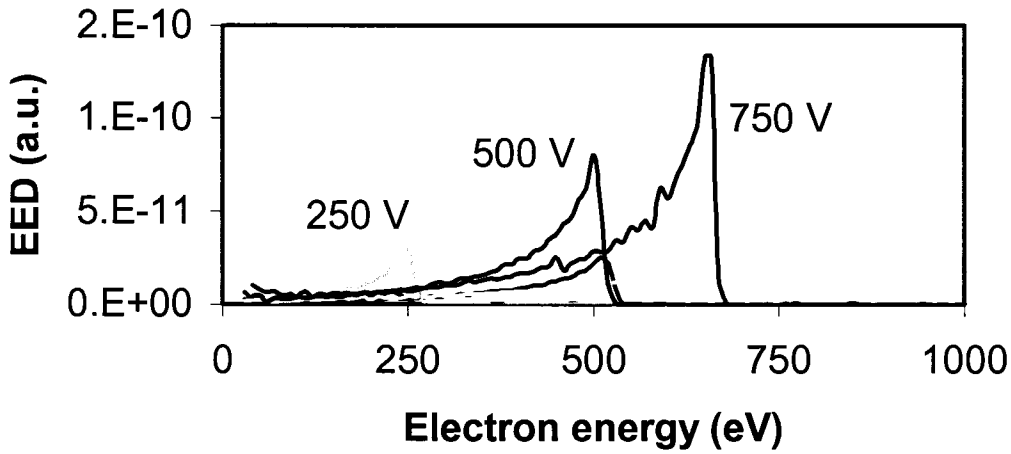

Figure 3.20 Measured electron beam energy spectra acquired with the retarding potential analyzer. ICP conditions are 10 mTorr CF_4, 250 W and 500 W in order of increasing EED magnitude. Electrode rf bias voltages (in rf Volts, peak-to-peak) are shown. Note that the electrode rf bias frequency is 4 MHz for the CF_4 data.

3.3 Conclusions

Electron beam energy spectra have been measured over a wide range of argon feedstock gas pressures, ICP powers, and cathode rf bias voltages. Beam operation was confirmed in other feedstock gases of interest to materials processing applications, specifically H_2 and CF_4.

Chapter 3 References

[1] K. E. Orlov and A. S. Smirnov, Proc. 14th Intl. Symp. on Plasma Chem., vol. 2, p. 807, Prague, Czech Republic (1999).

[2] D. M. Shaw, M. S. Thesis, Colorado State University, Fort Collins, Colorado (1999).

[3] L. Knipp, M. S. Thesis, Colorado State University, Fort Collins, Colorado (1995).

[4] K. Köhler, J. Coburn, D. E. Horne, E. Kay, and J. H. Keller: J. Appl. Phys. **57** 59 (1985).

[5] P. Gill and C. E. Webb: J. Phys. D **10** 299 (1977).

[6] J. Mathew, R. A. Meger, R. F. Fernsler, and J. A. Gregor, Rev. Sci. Instrum. **67**, 2818 (1996).

[7] V. A. Godyak, R. B. Piejak, and B. M. Alexandrovich, J. Appl. Phys. **73**, 3657 (1993).

[8] I. D. Sudit and R. C. Woods, J. Appl. Phys. **76**, 4488 (1994).

CHAPTER 4

ELECTRON BEAM ENERGY SPECTRA MODELING

4.1 Electron beam energy spectra model

To gather insight into the measured transmitted electron beam energy spectra, a simple model is developed. Figure 4.1 shows a schematic outline of the model. Several simplifying assumptions are made in the model. The bulk plasma is treated only as a source of ions to the rf biased cathode. In the model, secondary electrons emitted from the electrode are instantly accelerated to the full instantaneous value of the sheath potential, and this calculated electron energy is compared to the electron energy spectra as measured 14 cm from the cathode. To a first approximation, at 2 – 20 mTorr argon pressure, and at electron energies above 100 eV, the mean free path for electron-argon neutral collisions, λ, is greater than the 14 cm distance between the cathode and the RPA. Therefore, any electron-neutral collisions which may occur in the bulk of the plasma may be neglected without effecting the model. Any other types of beam-plasma interactions such as two stream instabilities, are also neglected. Nevertheless, the model shows good agreement with the measured electron beam energy spectra as shown below.

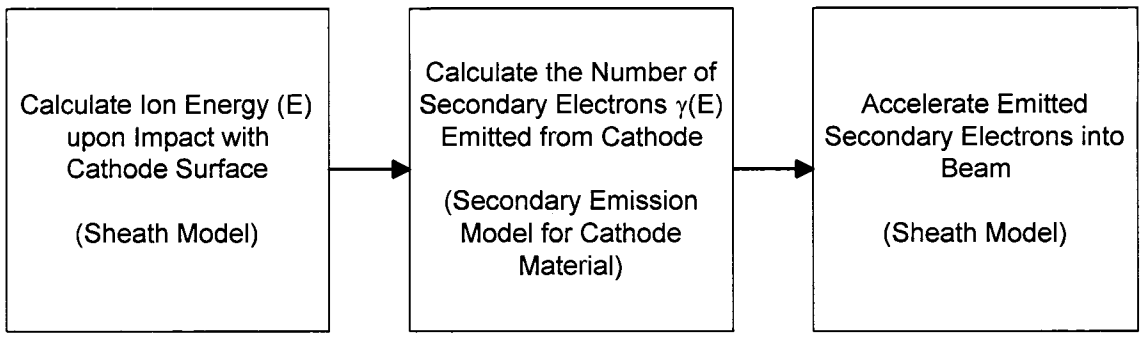

Figure 4.1 Outline of the electron beam energy spectra model.

The standard capacitive rf sheath models of Lieberman,[1] Godyak and Sternberg,[2] or Gierling and Riemann[3] are not used herein. These sheath models are more accurate in the conventional low electron density ($n_e \sim 10^9$ cm^{-3}) parallel plate capacitive discharge configuration, where the maximum sheath thickness is relatively large. In the wide sheath case, individual ions tend to respond only to the average DC potential of the sheath. Instead a slightly modified version of the collisionless Child-Langmuir rf sheath model of Field et al.[4] is chosen. This model allows ions to respond to the time-varying potential of the narrow rf sheath width typical of the higher plasma electron density ($n_e \sim 10^{11}$ cm^{-3}) ICP conditions presented herein.

The time varying sheath width d(t) is calculated by inserting the rf electrode voltage V(t) in for the DC electrode voltage in the Child-Langmuir sheath thickness equation:

$$d(t) = \frac{\sqrt{2}}{3}\lambda_{De}\left(\frac{4V(t)}{T_e}\right)^{3/4} \qquad \text{(eqn.1)}$$

where $\lambda_{De} = 740(n_s/T_e)^{1/2}$ is the electron Debye length in cm at the plasma-sheath interface, V(t) is the rf sheath voltage in Volts, T_e is the bulk plasma electron temperature in eV, and the sheath edge electron density n_s (cm^{-3}) is estimated to be 50% of the measured bulk plasma electron density n_e, $n_s \approx 0.5n_e$. The rf sheath voltage V(t) is assumed to be purely sinusoidal (harmonic free) and equal to the applied electrode rf voltage V(t) with a negative DC bias voltage equal to the rf voltage amplitude (peak to ground). The sheath electric field in V/cm acting on the ion at position x as it moves across the sheath is determined by inserting the time varying sheath thickness d(t) and voltage V(t) in the standard the DC Child-Langmuir equation:

$$E(x) = \frac{4}{3}\frac{V(t)}{d(t)}\left(\frac{x}{d(t)}\right)^{1/3} \qquad \text{(eqn.2)}$$

where all terms in equation 2 have been previously defined. It should be noted that this model is not self-consistent since the DC Child-Langmuir sheath assumes a temporally constant DC ion flux to the electrode, and our modulation of the sheath thickness forces the ion flux to vary with time inconsistently with the imposed field. Nevertheless, this model is straightforward to implement and fits the measured experimental data relatively well, as shown below.

Ions move from the bulk plasma towards the sheath in a presheath region and enter the sheath with the Bohm velocity[5] (u_B) and a superimposed random Maxwellian velocity distribution representing the ions thermal energy. It should be noted that changing the ion's Maxwellian temperature has very little effect on

the outcome of the model, since in general the ion thermal velocity is much less than the ion velocity in the sheath. When the ions enter the sheath, they are accelerated by the sheath electric field and impinge on the electrode. Figure 4.2 shows a schematic diagram of the model's ion trajectory and energy calculation routine. Upon impact with the electrode surface, secondary electrons are created. The secondary electron emission coefficient $\gamma(E)$ of the electrode surface is a function of incident ion energy and the surface material. For all calculations in this chapter, 2,000 ions are accelerated through the rf sheath. The ions enter the sheath at 100 equal phase intervals ($2\pi/100$) of the rf cycle for 20 rf cycles as shown schematically in Figure 4.3. The MatLab code used for the electron beam energy spectra model is listed in Appendix 1.

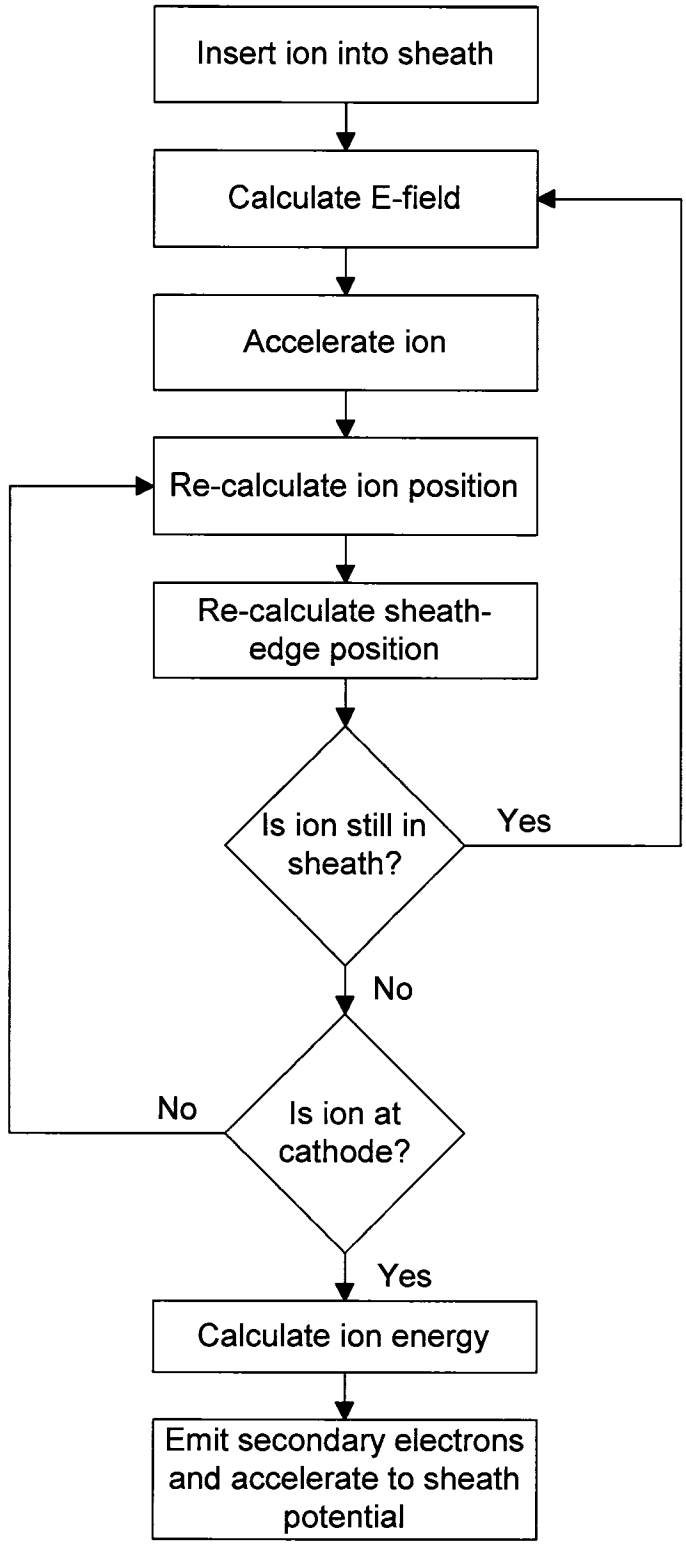

Figure 4.2 Schematic flow chart of the ion energy portion of model.

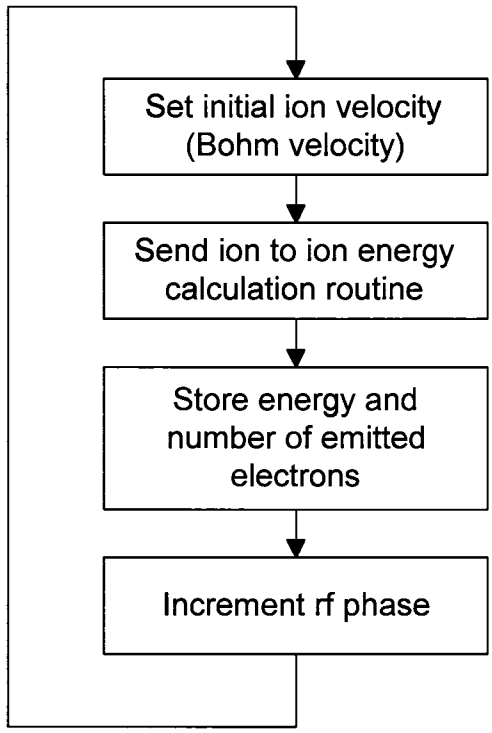

Figure 4.3 Schematic diagram of the entire electron beam energy spectra model. The model runs for 20 rf cycles and the rf phase is incremented by $2\pi/100$ each step.

In the simple linear model for ion-induced secondary electron yield from the Al_2O_3 electrode, γ increases monotonically from 0 to 1 as incident ion energy increases from 0 to 1000 eV[5] as shown in Figure 4.4. Secondary electrons are accelerated to the instantaneous sheath potential upon emission, eV_{sheath}. Figure 4.5 shows a sample ion trajectory through the sheath. Herein, the low energy (0 ~ 30 eV) portion of the electron beam spectra is neglected since it is difficult to distinguish from the background high energy tail of the bulk ICP electrons in the RPA electron beam energy spectra measurement.

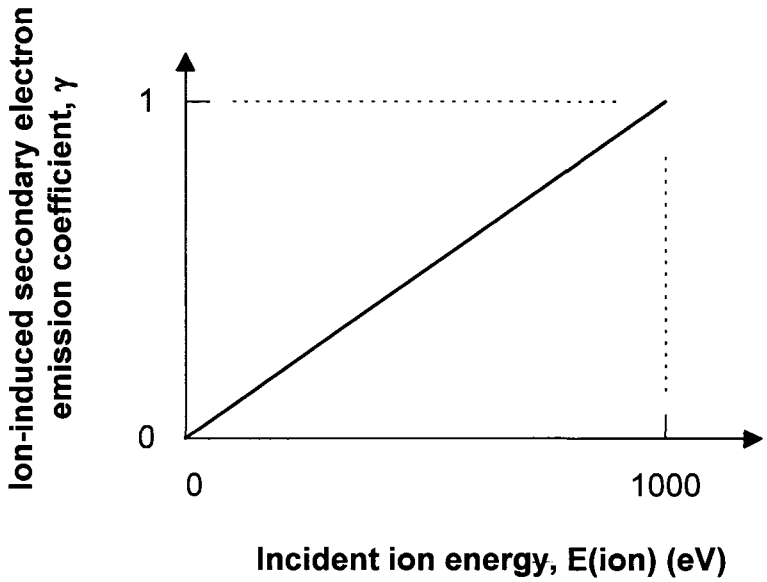

Figure 4.4 Linear model of secondary electron emission coefficient $\gamma(E)$ = (emitted secondary electrons) / (incident ions) for Al_2O_3. From Grais and Marcos, Jpn. J. Appl. Phys. 35, 5836 (1996).

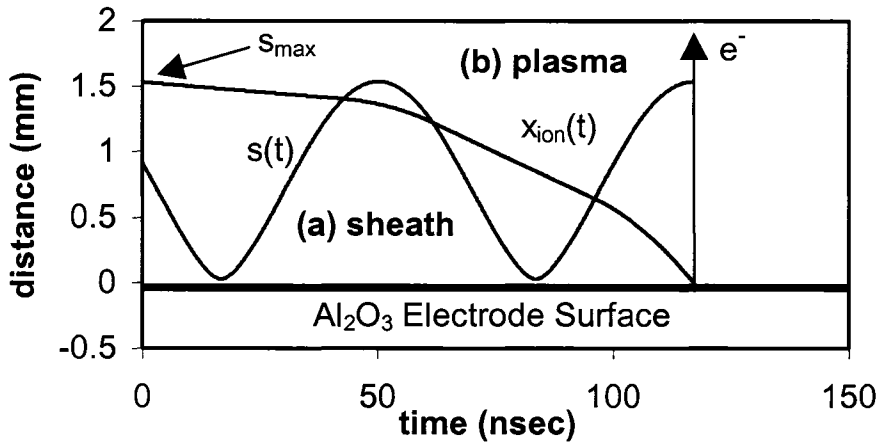

Figure 4.5 Sample modeled ion trajectory $x_{ion}(t)$ through the time varying sheath s(t). Calculation of the individual ion trajectory is shown schematically in Figure 4.3. Region (a) under s(t) is inside the sheath, region (b) is in the plasma, and s_{max} is the maximum extent of the plasma-sheath interface into the plasma region. Secondary electron emission and acceleration is shown as well. In this example, the emitted secondary electron is accelerated to approximately the maximum (negative) sheath potential. Modeled conditions are 5 mTorr Ar pressure, $n_e = 23.9 \times 10^{11}$ cm^{-3}, $T_e = 2.83$ eV, and $v_{rf} = 570$ V(p-p). Note that in the example shown, the ion takes about 1½ rf cycles (at 13.56 MHz) to cross the sheath.

The model uses five experimentally measured input parameters: electron temperature T_e in eV units, plasma electron density n_e in cm^{-3} units, applied electrode rf bias in V(peak-to-peak) units, ion mass in a.m.u., and rf frequency in Hz. The modeled electron energy spectra is given in arbitrary units only, due to the uncertainty in the exact values to be used in the secondary electron emission $\gamma(E)$ model of Figure 4.4. Nevertheless, as long $\gamma(E)$ is a linear function of E, which is a good assumption according to Grais and Marcos, the linear modeled electron energy spectra should be reasonable, even though the relative value of the magnitude is uncertain.

Due to the experimental uncertainty in the magnitude of both the modeled and measured electron energy spectra, the modeled spectra and measured spectra are fitted to one another by normalization of the peak values. Determination of the actual magnitudes of both modeled and measured electron beam energy spectra would be interesting work, at the added expense of orders of magnitude of increased complexity.

4.2 Electron beam energy spectra modeling results

4.2.1 Argon feedstock gas

In this section, the modeled and measured electron beam energy spectra are compared using argon as the feedstock gas. In general, the model captures the fundamental trends in the measured electron beam energy spectra over the range of operating conditions utilized herein. Considering the simplicity of the rf sheath model and the extreme difficulty of numerically modeling rf sheaths under the given plasma conditions, the model is in fact surprisingly successful. In Figures 4.6 and 4.7 below, the modeled results are compared to measured electron beam energy spectra at several typical argon ICP and cathode bias conditions covering the complete experimental range.

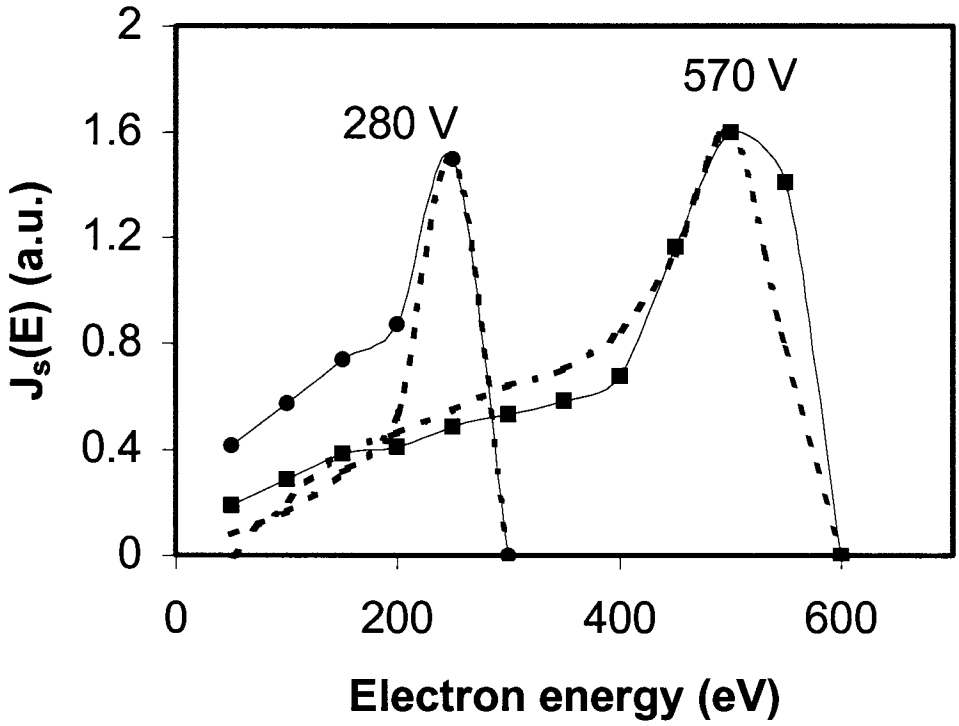

Figure 4.6 Modeled electron beam energy spectra (dashed lines) compared to measured electron beam energy spectra points. Experimental conditions are 20 mTorr Argon and 500 W applied to the ICP.

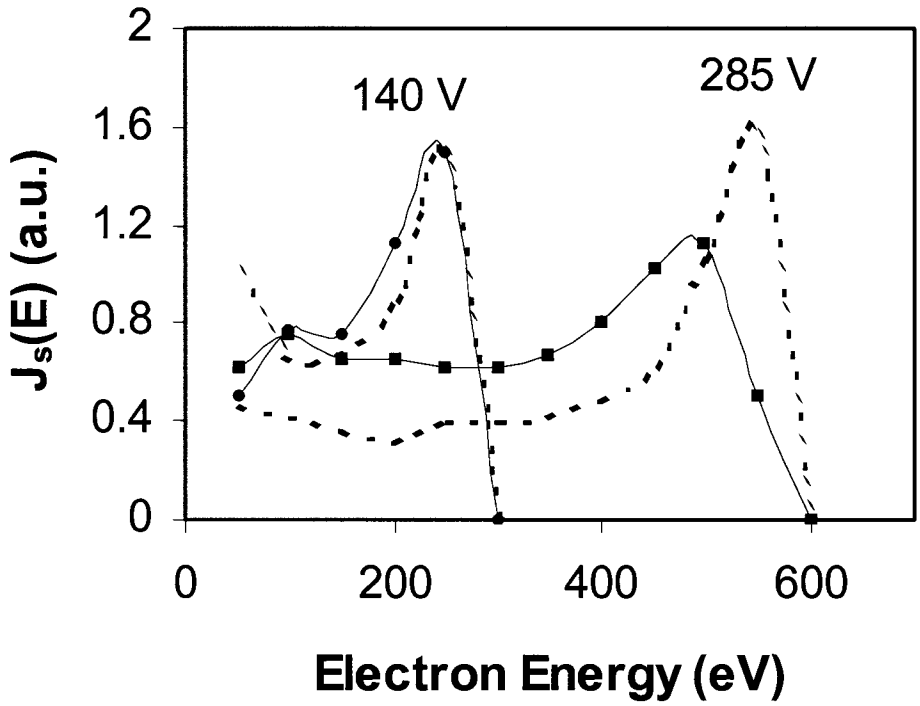

Figure 4.7 Modeled electron beam energy spectra (dashed lines) compared to measured electron beam energy spectra points. Experimental conditions are 2 mTorr argon and 125 W applied to the ICP.

While the match between model and experiment is generally good, the best fit is found at the two extremes of operating conditions, i.e., where the sheath is either widest and lowest voltage or narrowest and highest voltage. These two conditions correspond to the simplest sheath modeling cases. For the wide, low voltage sheath case, the ions take several rf cycles to cross the sheath, and all ions gain something like the average or DC sheath potential. Lieberman has developed a simple analytical model accurate for cases where the ion takes many rf cycles to cross the sheath. For the case of a narrow, high voltage

sheath, the ions traverse the sheath rapidly (in much less than one rf cycle) and gain near the instantaneous sheath potential at the time they enter the sheath. Metze, Ernie, and Oskam have developed a model that describes ion motion through the sheath in these conditions. In either case, the result of the model developed herein is to give the ions roughly the same energy and phase distributions as predicted by either Lieberman or MEO, although it should be noted that all experimental work performed herein is outside the conditions of either model. Figure 4.8 sketches the expected electron bean energy spectra for both the Lieberman and the MEO sheath model. Note the similarity to the measured and modeled spectra shown in Figure 4.7 to the sketched spectra using the Lieberman model, and the similarity of the measured and modeled spectra shown in Figure 4.6 to the sketched spectra using the MEO model.

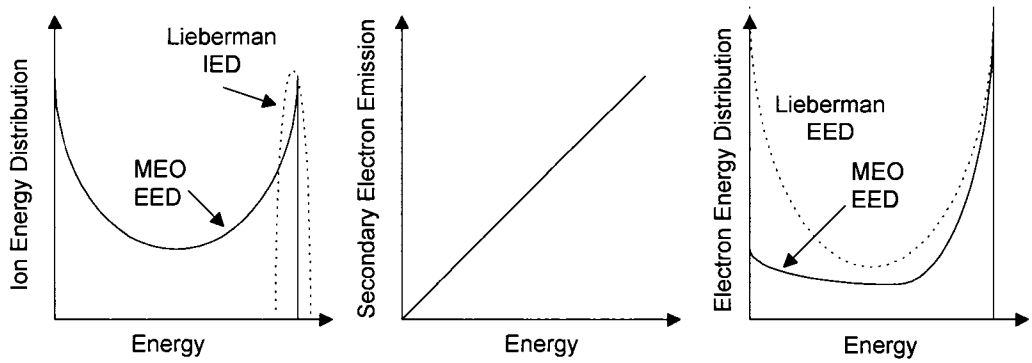

Figure 4.8 Sketch of the expected modeled electron beam energy spectra using the well known sheath model of (a) Lieberman for wide, low voltage rf sheaths, and (b) the MEO model for high voltage, narrow rf sheaths. Case (a) compares to, for example, the 125 W, 5 mTorr case of Figure 4.7, while case (b) compares well to, for example, the 500 W, 20 mTorr case of Figure 4.6.

Cases similar to the illustration shown in Figure 4.5, where the ion takes about one or two rf cycles to cross the sheath, is where the simple rf sheath

model probably tends to break down. Applying rf potential variations to the simple DC Child-Langmuir sheath model does not self-consistently treat the relationship between spatial charge distribution and spatial sheath potential variation, the calculated ion energy and phase distribution is probably most affected in the middle range of sheath conditions encountered. Nevertheless, even in the mid-range, the model gave results that indicated a good understanding of the physical operation of the electron beam. Further work on a more detailed and physically accurate sheath model would be an interesting, albeit difficult, study.

4.2.2 Hydrogen feedstock gas

As a further test of the electron beam energy spectra model accuracy, an attempt to simulate the measured EED in H_2 feedstock gas was undertaken. Both H^+ (M^+ = 1 a.m.u.) and H_2^+ (M^+ = 2 a.m.u.) ions were included in the model independently, and measured n_e and T_e values were used. The magnitude of the simulated EED's calculated for both ion species was adjusted arbitrarily in an attempt to fit the modeled EED to the measured EED data. The results are shown in Figure 4.9.

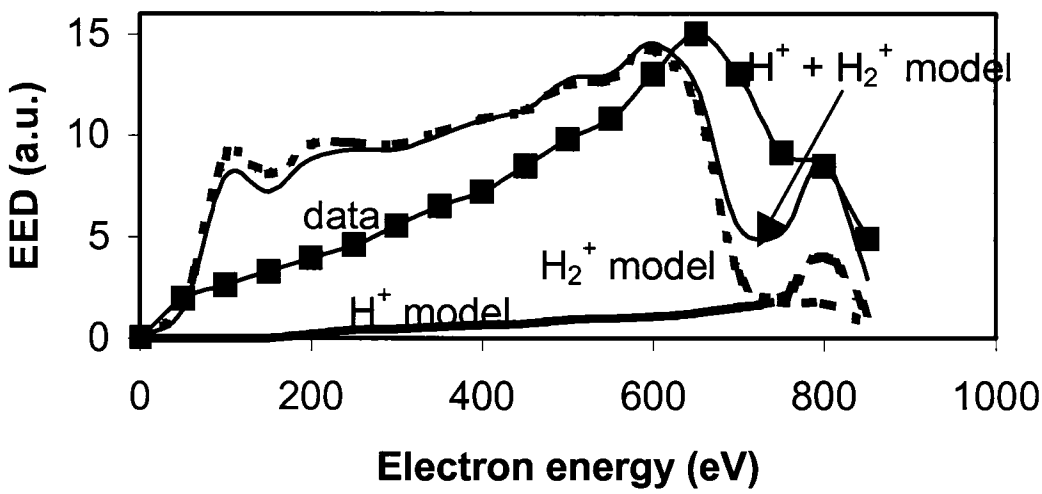

Figure 4.9 Modeled electron energy distribution in H_2 feedstock gas. Experimental conditions are 20 mTorr H_2, 500 W ICP power, and 850 V cathode bias voltage at 13.56 MHz. The model uses two ion species, H^+ and H_2^+. Each ion is modeled independently, and the results are combined. The solid squares represent experimental data. While the match between the modeled and experimental data is less than perfect, the model may explain the tendency for the reduced energy of the main peak and the smaller peak or shoulder near the cathode bias potential.

While the results of the simulation in Figure 4.9 do not show perfect agreement with the measured EED, the two principle features are at least partially captured. First, the main peak in the measured EED is at about 650 eV, lower than the 800 eV peak in data taken in similar conditions in other gases. The model suggests that this lower energy peak is the result of the low mass H^+ ions. The second feature captured by the simulation is the shoulder on the peak in the measured EED at about 800 eV. The model suggests that the shoulder is caused by the secondary electron emission caused by H_2^+ primary ions. While by no means conclusive, the crude agreement between the measured and

modeled EED in H2 feedstock is encouraging, and suggests the need for future work and refinement of the simulation.

4.3 Conclusions

A crude simulation has been developed to explain the measured electron energy distribution produced by the rf biased secondary electron beam source. The model shows good agreement with measured EED spectra in argon feedstock gas, suggesting that interaction the EED is a function of rf sheath conditions. Furthermore, the similarity between the measured and modeled EED suggests that interactions between the electron beam and the plasma are minimal over the range of experimental conditions investigated. Finally, although the agreement between the model and simulation was less than perfect for H_2 feedstock gas, the model may be used to understand the general behavior of the EED in gases other than Ar.

Chapter 4 References

[1] M. A. Lieberman, IEEE Trans. Plasma Sci. **16**, 638 (1988).

[2] V. A. Godyak and N. Sternberg, IEEE Trans. Plasma Sci. **18**, 159 (1990).

[3] J. Gierling and K.-U. Riemann, J. Appl. Phys. **83**, 3521 (1998).

[4] D. Field, D. F. Klemperer, P. W. May, and Y. P. Song, J. Appl. Phys. **70**, 82 (1991).

[5] K. I. Grais and M. L. Marcos, Jpn. J. Appl. Phys. **35**, 5836 (1996).

CHAPTER 5

REDUCTION OF OXIDE MICROTRENCHING VIA ELECTRON-ASSISTED PLASMA ETCH

5.1 Introduction to charge induced pattern transfer issues

In plasma pattern etching, positive ions accelerated to the substrate by the rf biased electrode sheath shown in Figure 5.1 provide directionality for forming vertical feature profiles. Figure 5.2 shows a close up sketch of the pattern etching process, using the example of silicon oxide etching.

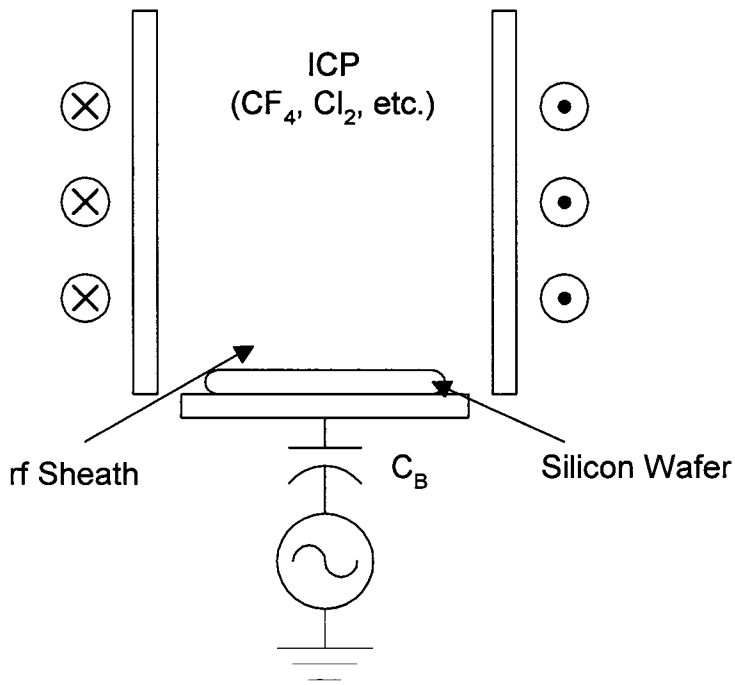

Figure 5.1 Schematic of a typical inductively coupled plasma (ICP) etch system using capacitive rf bias to set the energy of the ions impinging on the etching wafer. The sheath accelerates ions from the plasma to the wafer surface to provide directionality to the etch process.

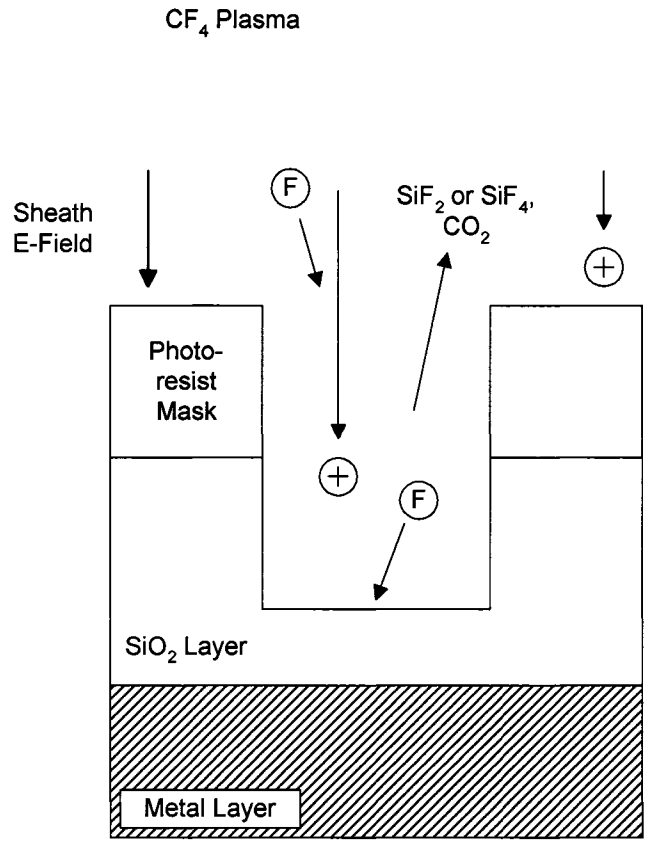

Figure 5.2 Close-up view of the fluorine-based silicon dioxide ("oxide") etch process. The ions accelerated by the sheath electric field to the etching SiO_2 layer increase the downward etch rate to provide directionality to the etch process.

Simultaneous to the ion impingement, plasma electrons, due to their random thermal motion, tend to impinge on the sidewalls near the top of the feature as shown in Figure 5.3.

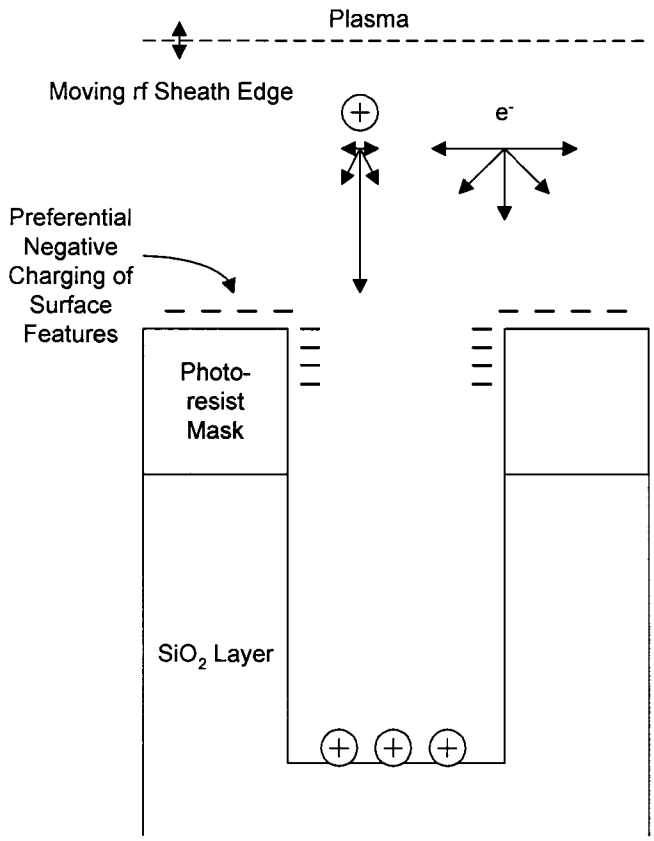

Figure 5.3 Schematic diagram showing the preferential negative charging of insulating surface features by plasma electrons and preferential positive charging of feature bottoms by the highly directional ions accelerated by the sheath.

Over the course of the etch process, the feature bottom charges positively and the sidewalls charge negatively, creating undesired local electric fields within the feature as shown schematically in Figure 5.4 (a). Subsequent ion trajectories tend to be deflected towards the sidewalls, resulting in increased ion flux and hence increased etch rate near the edges of feature bottom, and decreased etch rate at the center as shown schematically in Figure 5.4 (b). As device feature sizes continue to decrease, the local electric field is becoming problematic by causing non-ideal etch profiles such as microtrenching in oxide[1,2] and notching in

polysilicon[3-7]. Recent theoretical work has even suggested that feature charging may lead to complete etch stoppage in high aspect ratio contact holes.[8]

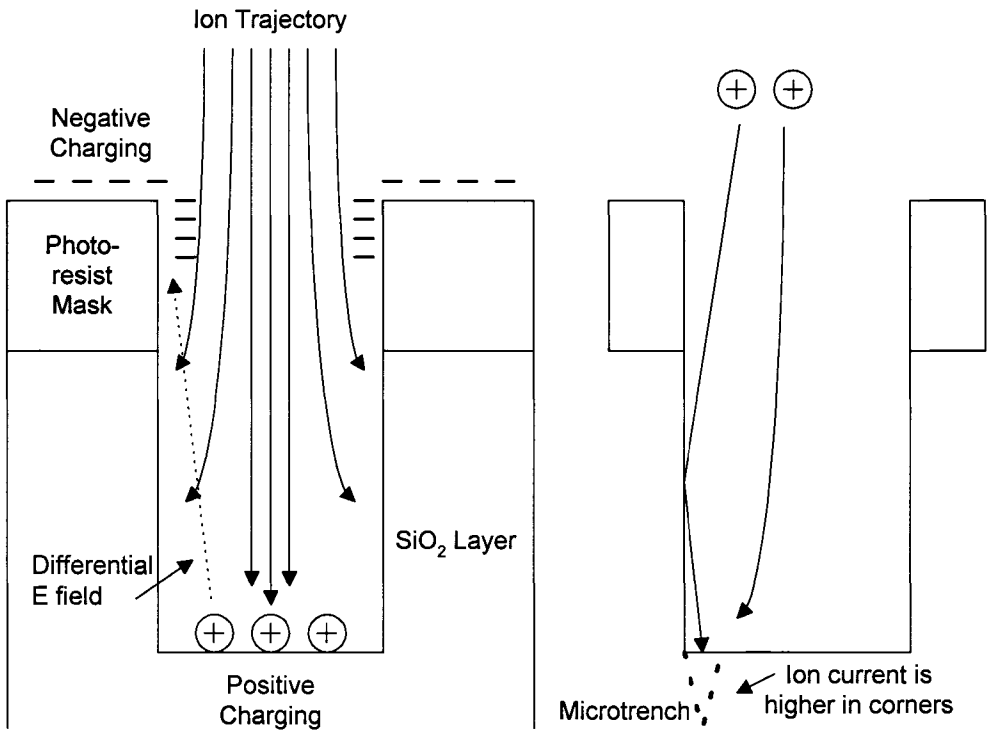

Figure 5.4 The preferential charge build-up shown in Figure 5.2 results in a differential electric field within the etching feature, which tends to deflect the trajectory of the impinging ions as shown. The result of the ion deflection is to increase ion current in the trench corners, increasing the etch rate locally and causing feature distortions such as "microtrenching."

5.2 Microtrenching in oxide etching

Figure 5.5 schematically illustrates an oxide trench profile near etch endpoint. Microtrenching has exposed the underlying silicon substrate near the bottom edges, leaving an oxide island in the center. Since the conducting silicon underlayer does not allow positive charge accumulation, ions tend to be further deflected towards the feature edges, making clearing of the oxide island difficult.

Frequently, when the etch time is extended in an attempt to remove the oxide islands (termed "overetching"), microtrenches are inadvertently transferred into the underlying silicon, causing device damage. In extreme cases, the oxide island remains even after overetching, causing high electrical contact resistance to the underlayer in the completed device. Therefore, a method to reduce charge buildup and the resulting microtrenching and oxide island formation within etching features is desirable.

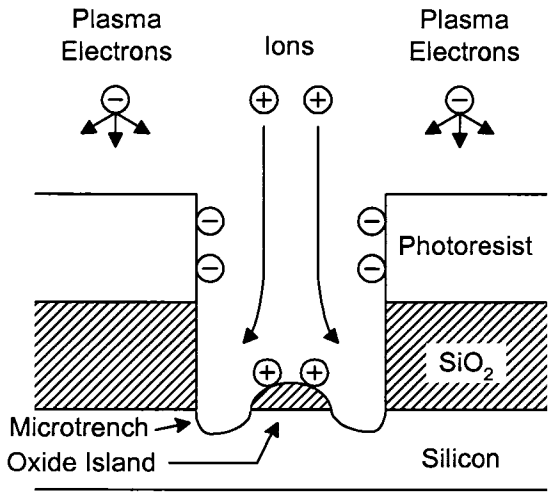

Figure 5.5 Schematic illustration of microtrench and oxide island formation near the etch endpoint in oxide feature etching.

Energetic electron flux from a hot tungsten filament incident on the etching substrate has been proposed to reduce notching during poly-silicon etching and RIE-lag during oxide etching.[9] Herein, the rf driven electron beam source is investigated for *in-situ* irradiation of the etching substrate to reduce microtrenching and island formation during oxide etching. Figure 5.6 schematically shows the addition of electron irradiation during oxide etching for charge neutralization. Energetic electron flux normal to the wafer surface

reaches the feature bottom and neutralizes the positive charge on the oxide island. The local electric field within the feature is reduced, and straighter ion trajectories are obtained. Therefore, more ideal etching profiles and reduced overetch time can be expected.

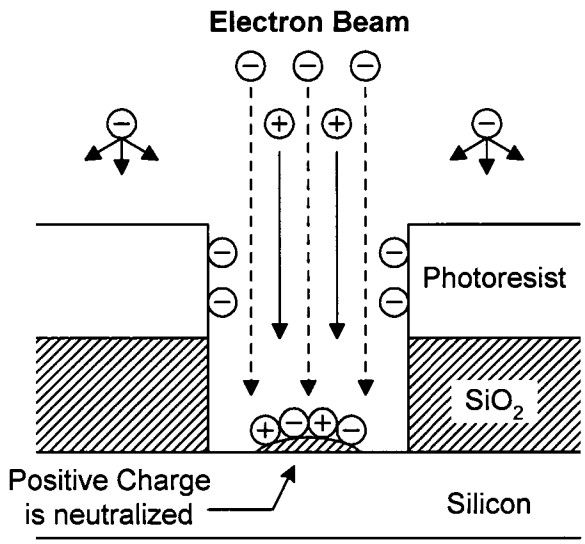

Figure 5.6 Electron beam irradiation during etching neutralizes positive charge buildup on the oxide island and reduces the local electric field inside the etching feature. The result is a more uniform ion flux distribution along the feature bottom, increasing etch rate uniformity and reducing microtrenching.

5.3 Experimental setup

Figure 5.7 shows a schematic drawing of the inductively coupled plasma (ICP) etching system used herein, with the electron beam source located 14 cm away from the wafer electrode. In contrast to the hot tungsten filament used in prior work[9], the cold cathode secondary electron beam source is fully compatible with reactive etch gases. Electron beam energy is set to 850 eV, and the wafer sheath rf (13.56 MHz) potential is set to 200 $V_{p\text{-}p}$. In contrast to most of the electron beam measurements in Chapter 3, the beam source rf bias frequency

used in the etching experiments is 4 MHz. The radio frequency of 4 MHz was chosen to avoid frequency dependent interaction between the beam and substrate biases. Electron beam energy spectra recorded with 4 MHz bias frequency (see Figure 3.21) appear similar to the spectra taken using 13.56 MHz bias, as discussed in Chapter 3. Plasma feedstock gas is 6 mTorr of CF_4:H_2 (10:1).

Oxide films on silicon substrates with 0.45 μm diameter hole patterns defined by photoresist masks are placed on the rf biased wafer electrode. Substrates are etched under identical plasma conditions both with and without electron beam irradiation. The wafer holder is water cooled to avoid overheating and melting of the photoresist mask.

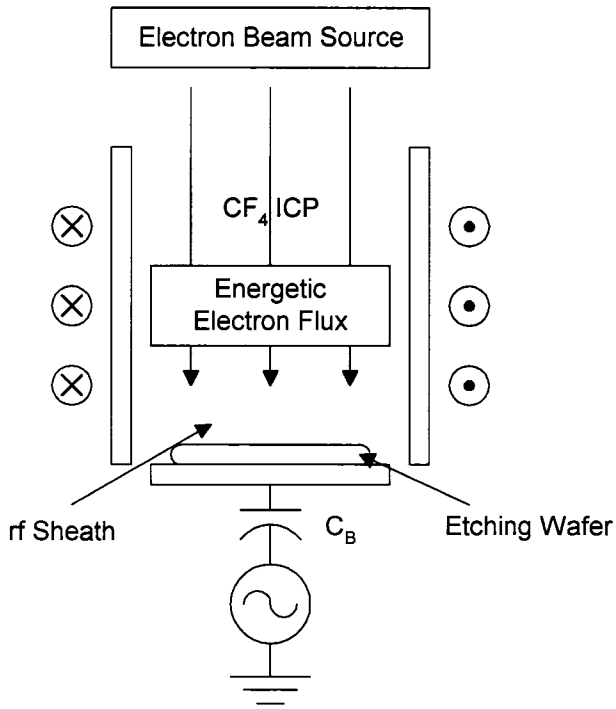

Figure 5.7 Schematic showing the addition of the electron beam source on a standard ICP etch system.

5.4 Experimental Results

Figure 5.8 illustrates the effects of the electron beam neutralization within the etching feature via scanning electron microscopic (SEM) imaging. Figure 5.8(a) shows an oxide contact hole near endpoint etched without electron beam irradiation. An oxide island and two deep microtrenches are clearly visible. The flatter bottom corners of the contact hole etched with simultaneous electron beam irradiation in Fig. 5.8(b) clearly shows reduced microtrench and oxide island formation.

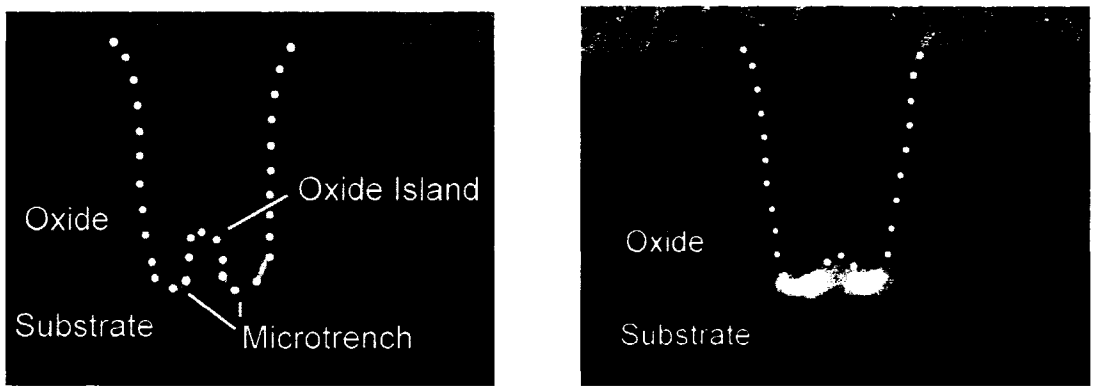

(a) (b)

Figure 5.8 SEM images of 0.45 μm oxide contact holes near etch endpoint. The feature edges are highlighted with a dotted line as a guide to the eye due to the difficulty in reproducing the SEM images. (a) Microtrenching and oxide island formation on the contact hole bottom are evident without electron beam irradiation. (b) Although still present, island formation and microtrenching are much reduced by simultaneous electron beam irradiation.

5.5 Simulation of electron beam reduction of microtrenching

A simplified 2D computer simulation, based on the previous work of Arnold and Sawin[1], is used to verify that the observed microtrench and oxide island reduction is due to charge neutralization by the electron beam irradiation. In the simulation, ions and electrons are incident on a trench-shaped feature with zero initial charge. The local electric field created as charge builds up is computed, and subsequent charged particle trajectories are deflected. Steady state conditions are obtained when the net charge flux to any dielectric surface becomes zero. In order to simulate the conducting substrate exposed near etch endpoint, the edges of the feature bottom are not allowed to charge up, while the center of the feature bottom can accumulate charge to replicate the insulating oxide island. The simulation is run both with and without the electron beam to study its effect on the ion trajectories.

The results of the simulation are shown in Figure 5.9. The solid line shows non-uniform ion flux distribution along the feature bottom when only ion and low energy plasma electron fluxes are considered. Incident ions are deflected towards the sidewalls by the electric field created primarily between the positively charged oxide island and the conducting substrate where charge accumulation does not occur. The non-uniform ion flux distribution results in increased etch rate at the feature bottom edges and reduced etch rate at the center, enhancing microtrenching and oxide island formation.

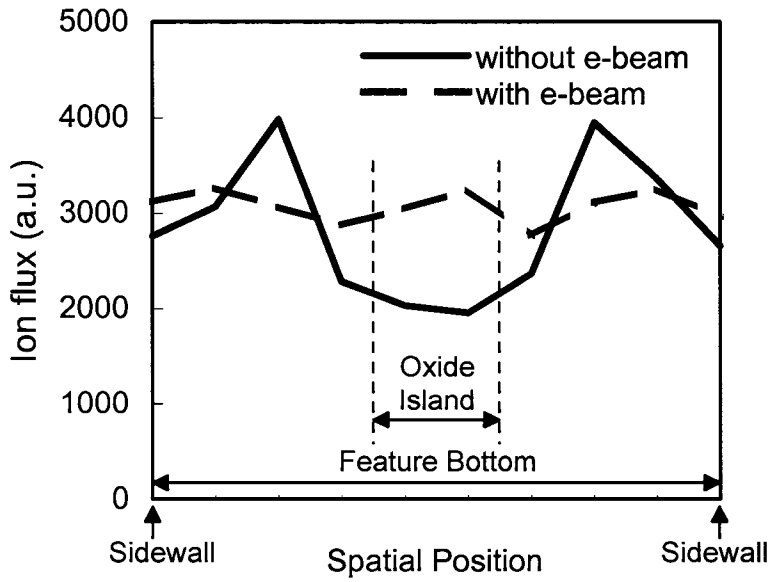

Figure 5.9 Simulated ion flux distribution reaching the oxide feature bottom near the etch endpoint with and without simultaneous directional electron beam irradiation. With no electron beam flux, the local electric field inside the etching feature deflects ion trajectories towards the edges. The local electric field is reduced due to charge neutralization on the oxide island with electron beam irradiation, resulting in a more uniform ion flux distribution.

When simultaneous electron beam irradiation is added to the ion and low energy plasma electron fluxes, the calculated ion flux distribution along the trench bottom becomes more uniform as shown with the dashed line in Figure 5.9. Here, positive charge neutralization by the energetic beam electrons incident on the oxide island reduces the local electric field inside the feature. The resulting ion trajectories are straighter, resulting in more uniform ion flux and implying a spatially uniform etch rate along the feature bottom. The results of our simple particle trajectory simulation agree well with the experimental etch profiles shown in the SEM images of Fig. 5.8.

In addition to the reduced ion flux uniformity in the case without electron beam irradiation, the simulation also indicates that the energy of the ions incident on the oxide island is reduced by the decelerating effect of the unintentional electric field. However, the ions incident on the conducting feature bottom edges maintain their initial energy. By reducing the unintentional electric field with electron beam irradiation, a more uniform ion energy distribution along the feature bottom is obtained. Although the ion flux distribution strongly determines the etch rate along the feature bottom, the incident ion energy distribution could also influence the local etch rate. We are currently studying the combined effects of both spatial ion flux variation and ion energy variations on the local etch rates.

5.6 Conclusion

In summary, we have explored charge neutralization using electron beam irradiation to reduce microtrench and oxide island formation during conventional plasma etching of oxide patterns. SEM images indicate that the technique

results in a dramatic reduction of microtrench and oxide island formation near the etch endpoint. A computer simulation of ion trajectories within the etching feature verifies that the charge neutralization reduces the unintentional electric field responsible for microtrench/oxide island formation. To our knowledge, this is the first experimental demonstration of the electron beam charge neutralization technique to reduce microtrench/oxide island formation during oxide etching.

Chapter 5 References

[1] J. C. Arnold, and H. H. Sawin, J. Appl. Phys. **70**, 5314 (1991).

[2] M. Schaepkens, and G. S. Oehrlein, Appl. Phys. Lett. **72**, 1293 (1998).

[3] T. Nozawa, T. Kinoshita, T. Nishizuka, A. Narai, T. Inoue, and A. Nakaue, Jpn. J. Appl. Phys. Part 1, **34**, 2107 (1995).

[4] T. Kinoshita, M. Hane, and J. P. McVittie, J. Vac. Sci. Technol. B, **14**, 560 (1996).

[5] N. Fujiwara, S. Ogino, T. Maruyama, and M. Yoneda, Plasma Sources Sci. Technol. **5**, 126 (1996).

[6] N. Fujiwara, T. Maruyama, and M. Yoneda, Jpn. J. Appl. Phys. Part 1, **35**, 2450 (1996).

[7] T. H. Ahn, K. Nakamura, and H. Sugai, Plasma Sources Sci. Technol. **5**, 139 (1996).

[8] J. Matsui, N. Nakano, Z. L. Petrovic, and T. Makabe, Appl. Phys. Lett. **78**, 883 (2001).

[9] A. K. Quick , University of Wisconsin-Madision, Ph.D. thesis, 1998.

[10] D. M. Shaw, M. Watanabe, H. Uchiyama, and G. J. Collins, Appl. Phys. Lett. **75**, 34 (1999).

[11] D. M. Shaw, M. Watanabe, G. J. Collins, and H. Sugai, Jpn. J. Appl. Phys. part 1, **38**, 4590 (1999).

CHAPTER 6

CONCLUSIONS AND SUGGESTIONS FOR FUTURE WORK

A new plasma-generated electron beam source using an rf biased, electrically insulating cathode with high secondary electron emission has been developed. The source allows control of the electron beam energy via the rf bias voltage on the cold cathode, and control of the electron beam current via the bulk plasma conditions (ICP power and gas pressure). Full characterization of the electron beam source was undertaken in argon gas. The peak beam energy is found to be directly related to the rf voltage applied to the cathode, and electron beam current is related to the ion density of the ICP providing ions to the source and the energy of the ions impinging on the cathode. The measured electron beam energy spectra show basic agreement with a simple model comparing the rf waveform applied to the cathode to the electron beam energy.

The electron beam is used to enhance pattern transfer fidelity in plasma etching of 0.45 μm contact hole patterns in silicon oxide films. Spatially non-uniform charge buildup in the contact holes as the etching process takes place tends to deflect incident ions towards the bottom edges of the holes, preferentially etching the edges at a higher rate than the hole centers and causing microtrenching. By irradiating the etching films with energetic electrons from the beam source, microtrenching was reduced, as seen using SEM

imaging. A simple model verifies that charge neutralization by the electron beam is responsible for microtrench reduction.

Some other potential applications for the electron beam are in assisting surface processes such as low temperature electron beam hardening and curing of polymers as well as electron beam assisted film deposition and etching. More esoteric potential applications might exist, such as electron beam excitation of wide area phosphor screens for intense backlighting of flat panel displays. The exploratory 3 cm diameter source used herein is also judged to be scalable to the larger diameters (> 30 cm) required for practical materials processing applications, since both prior art ICP and capacitive rf discharges both are easily scaled to these dimensions with ±5% uniformity.

The potential for future work with the electron beam source may be broken into two main categories. First, the beam itself should be understood more fully. Absolute measurements of the electron beam current density should be undertaken, rather than the relative measurements presented herein. Understanding the relationship between the secondary electron emission coefficient $\gamma(E)$ of the cathode surface and different gases such as CF_4 would be useful to gain better process control in the particular process of interest. Very little data exists covering $\gamma(E)$ in the literature. Adding a more complex sheath model to the electron beam energy spectra model might allow for better understanding of $\gamma(E)$ by comparing the modeled results with experimental data.

Although the good agreement between the experimental beam energy spectra measurements and the simple model tend to give confidence that little

beam-plasma interaction takes place in the experimental range studied herein, more detailed studies to confirm this would be of interest. Also, knowing the conditions when beam-plasma interaction will begin will help develop the process window for some other applications of interest.

The second main category of future work is in the area of electron beam assisted process development. While the pattern transfer fidelity enhancement shown in Chapter 5 is very promising, it is only the "tip of the iceberg." Developing a process which is capable of reducing microtrenching and/or providing better etch selectivity in 0.1 μm and smaller contact holes would be of great interest to the semiconductor industry. Scaling the source to 30 cm diameter for compatibility with modern plasma etch chambers will be required if electron beam assisted etching is to find its way into industrial application. Testing of the source in chlorine-based gas chemistries is needed in order to investigate pattern transfer issues such as notching in poly-silicon etching.

APPENDIX 1

CODE FOR ELECTRON ENERGY SPECTRA CALCULATIONS

EBEAM.M

```
%       This program calculates the ion energy distribution and electron energy
%       distribution for given ICP and cathode rf bias conditions.

clear;  %clear all variables from memory

%       For operation, the following parameters must be input:

ionvel=1000;    %ion velocity entering the sheath (m/sec)
                %for a Maxwellian distribution = exp(-vinit/ionvel)

ionnum=2000;    %total number of ions in the simulation

for N=1:ionnum,%loop for each ion in simulation

  vinit=exprnd(ionvel);   %pick initial ion velocity entering the
                          %sheath, using a Maxwellian distribution

  trajectory;     %run ion trajectory simulation
                  %"trajectory" returns the incident ion energy on cathode
                  %and the sheath potential at the instant of ion impact

  elenum(N)=E;            %ion energy on cathode returned from "trajectory"
                          %Assume that gamma(E)=E, which is linear function
                          %So we have "E" secondary electrons emitted

  eleenerg(N)=Volts;      %set energy of the above emitted electrons
                          % = instantaneous sheath voltage "Volts"
                          %where "Volts" is returned from "trajectory"

end     %the end of the for loop

save elenum;    %save the file to working directory on disk drive
save eleenerg;  %save the file to working directory on disk drive

%quit;

%plot out the ion energy distribution (IED) upon completion of program

%plot(hist(elenum,20)); %plots IED;
```

TRAJECTORY.M

```
%This program calculates the trajectory of an individual ion entering
%the sheath until it hits the cathode.

%The program returns the ion energy on the cathode and the sheath
%voltage at the time of impact

%The following parameters need to be input for operation:

Te=5.96;  %electron temperature in eV

ne=9.7*10^10;  %electron density in cm-3

Vsheathmax=425;  %rf cathode voltage, Volts peak-to-ground

Mi=4;   %ion mass in amu

f=13.56*10^6;  %set rf frequency in hertz

%----------------------------------

M=Mi*1.67*10^-27;  %Ion mass, kg

uB=(9.8*10^3)*((Te/Mi)^0.5);     %calculate Bohm velocity, meters/sec

LDe=7.4*((Te/ne)^0.5);  %calculate Debye length in meters

lmax=0.4714*LDe*((4*Vsheathmax/Te)^0.75); %calculate max sheath width, meters

timestep=6*10^-11;  %timestep for equations of motion, sec

%stuff for standalone operation

%N=0;
%vinit=1000;

%clear variables in loop

clear v;
clear d;
clear Vsheath;
clear l;
```

```
v(1)=uB+vinit;   %set initial velocity in m/sec
                 %this value comes from the calling program

d(1)=lmax;  %set initial position at max sheath extent

phi=(N/50)*pi;  %set initial phase of sheath in rad, N from calling program

e=1.6*10^-19;  %elementary charge

%run the program

lo=lmax/((2*Vsheathmax)^0.75);  %sheath constant

for I=2:50000,
  %define sheath voltage
  Vsheath(I)=1.01*Vsheathmax+Vsheathmax*sin(2*pi*f*I*timestep+phi);
  %define sheath location
  l(I)=lo*((Vsheath(I))^0.75);
  if l(I)>d(I-1)-v(I-1)*timestep; %if ion in sheath then accelerate
    %adjust velocity:
    v(I)=v(I-1)+(4/3)*(e/M)*((Vsheath(I)/l(I))*(((lmax-d(I-1))/l(I))^0.33)*timestep);
    %adjust position:
    d(I)=d(I-1)-v(I)*timestep;
    if d(I)<=0;  %stop loop when ion hits cathode
      %calculate ion energy at cathode in eV, return to calling program
      E=0.5*(M/e)*v(I)^2;
      %Sheath voltage associated with this ion in Volts, return to calling program
      Volts=Vsheath(I);
        break;
              end      %end of stop loop
  else  %ion is not in sheath
    %no acceleration, keep old velocity:
    v(I)=v(I-1);
    % adjust position:
    d(I)=d(I-1)-v(I)*timestep;
  end    %end of if in sheath
end      %end of for loop


%stuff for standalone operation
%Volts
%E
%plot([1:length(d)],d,[1:length(I)],I)
```

ELESORT.M

```
%this program sorts the electrons into energy bins and plots the results
clear;
load elenum;     %load the saved electron number file
load eleenerg;   %load the saved electron energy file
for J=1:20, %step through energy bins
  enerbin(J)=0;  %set energy bin to zero
  for I=1:2000,  %step through energy vector (eleenerg)
    if eleenerg(I) >= J*50  %check if energy is greater than min. in bin
      if eleenerg(I) < (J+1)*50  %check if energy is less than max. in bin
        enerbin(J) = enerbin(J) + elenum(I);  %add number of electrons at eleenerg to bin
      end
    end
  end
end
plot(enerbin,'co:');  %plot eed
```